Dissolution kinetics of trapped air in a spherical void: Modeling the long-term saturation of cementitious materials

Scott C. Smith, Matthieu Vandamme, Kimberly E. Kurtis

Dissolution Kinetics of Trapped Air in a Spherical Void: Modeling the Long-Term Saturation of Cementitious Materials

Scott H. Smith[1], ssmith314@gatech.edu

Matthieu Vandamme[2], matthieu.vandamme@enpc.fr (corresponding author)

Kimberly E. Kurtis[1], kkurtis@gatech.edu

[1] Georgia Institute of Technology, Atlanta, GA

[2] Laboratoire Navier, Ecole des Ponts ParisTech, Champs-sur-Marne, France

Abstract:

The saturation of air-entrained cementitious materials governs their resistance to freeze-thaw cycles. Upon immersion in water, water is sucked in the capillary porosity and part of the air initially present is trapped. This trapped air slowly dissolves and diffuses outward, leading to a slowly increasing saturation. Building on efforts in fields ranging from gas-liquid interfaces to multi-phase transport and cement sciences, a model is derived to describe the governing physics behind the long-term saturation rate in immersed cementitious materials due to the dissolution and diffusion of trapped gaseous air in a spherical air void. We model how liquid water continuously enters a single air void and how various material properties influence the time to complete dissolution of air trapped in the spherical void. The relative influence of advection, diffusion, and various materials properties are studied and the model results are found to agree with imaging studies and theoretical models.

Keywords: A. Kinetics, C. Transport Properties, E. Modeling

Declarations of Interest: None

1.0 Introduction:

In recent years, the critical saturation (S_{cr}) of cementitious materials has gained significant attention [1–5] due to its ability to predict when freeze-thaw-induced damage will initiate [2,6–8]. The time it takes for fully water-immersed concrete specimens to reach S_{cr}, referred to as time to critical saturation (t_{cr}), has recently been incorporated in AASHTO PP84 [9] to ensure a minimal service life in freezing-and-thawing environments. Beginning in [1] and extended in [2,4], it was recognized that experimentally obtained long-term saturation rate values can be used to estimate t_{cr} assuming an experimental S_{cr} value of 85% [2,6,8]. The long-term saturation of air-entrained cementitious materials, idealized as a heterogenous porous solid with dispersed spherical voids as shown in Figure 1a, refers to the slow and time-dependent process in which air-entrained cementitious material move from its matrix saturation, S_m, to its critical saturation S_{cr} [10]. Although significant progress has been made experimentally in understanding how S_{cr} can be leveraged as a service-life assessment tool, the fundamental mechanism by which single air voids in cementitious materials become slowly water-filled needs to be better understood theoretically.

The long-term saturation rate, S_2, is hypothesized to occur due to the dissolution and diffusion of compressed air in the entrapped and entrained air voids [2,10], as shown in Figure 1b. Once the material reaches its matrix saturation (i.e., when the capillary porosity of the cement matrix is saturated with liquid water), trapped air is compressed by the Laplace pressure resulting from surface tension effects which induces dissolution of the compressed air into the fluid within or in the vicinity of the air void [10,11]. This dissolved air slowly diffuses outward while liquid water

flows toward the air void, resulting in a slowly increasing saturation of the air void and the complete dissolution of the initially trapped air [11]. However, despite previous efforts, the coupled mechanism of dissolution, diffusion, and advection that lead to the saturation of a single air void, or as group of air voids (i.e., a realistic 3D system), has yet to be clearly expressed in a single, physics-based model [3]. For the purposes of the efforts presented, the theoretical water-filling mechanisms for a single air void surrounded by a cement paste shell will be developed.

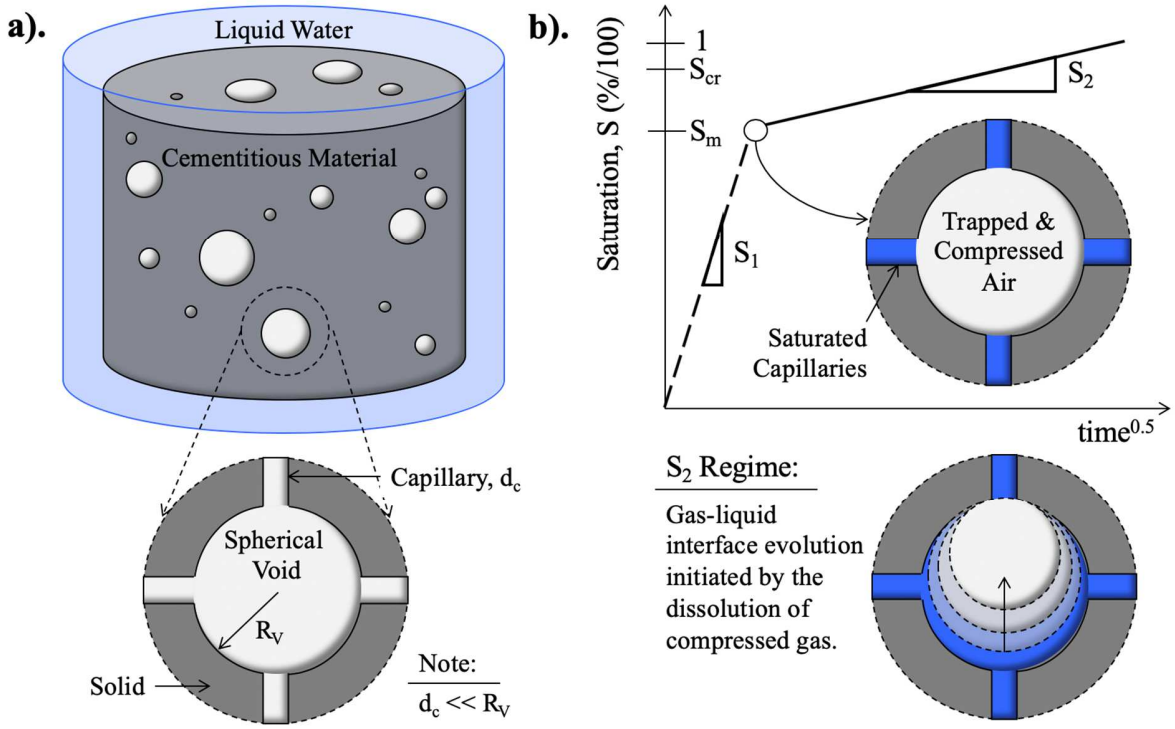

Figure 1 – a). Idealized air-entrained cementitious material system that is fully immersed in water and single air void-shell system, at the moment when it is immersed b). standard bi-linear saturation curve for air-entrained cementitious materials [2] and idealized saturation behavior of the air-void shell system which is initialized by the compression of gaseous air and its resulting dissolution into the surround saturated capillary porosity [10].

In effort to ensure that the governing physics of how air voids become increasingly water-filled is captured, theoretical and experimental efforts made in various fields, ranging from macro-scale investigations of water-immersed mortars [12] to micro-fluidic studies on the dissolution of trapped gas bubbles [13], are critically reviewed. The review will first assess macro-scale phenomena and progressively move in the direction towards the void scale –as the long-term saturation of cementitious materials occurs due to the slow saturation of large porosity [10,14] (i.e., spherical air voids which range on the order from 10μm to 1mm in radius and are interconnected by irregular capillary pores which are orders of magnitude smaller [15]). Additionally, fundamental questions are identified which are central to understanding the governing dynamics of time-to-full-dissolution of air within a single spherical air void.

With respect to the model's derivation, a representative air-void and hardened shell system is first defined and the necessary geometry to describe the temporal evolution of a realistic water-air interface during saturation is detailed. As shown in Figure 1b, it is assumed that all of the capillary pores which connect the spherical air voids to each other, and the surface, are completely water saturated – suggesting that any air-void-and-shell system is at its matrix saturation. Attention is given to initial system assumptions, ensuring that the initial amount of trapped air within a void is known. Following this, mass balance equations for liquid water and dissolved air within the porous hardened cement paste shell are developed in addition to the mass conservation of gaseous air and liquid within the spherical air void. The result is a set of four coupled partial differential equations which are solved using various state equations and

assumptions which treat the gaseous air as ideal, the liquid water as incompressible, and the entire system as isothermal.

Solutions to the set of equations – called the single void dissolution kinetics (SVDK) model - are then used to determine the saturation kinetics of the air void and the relative importance of the various transport mechanisms (i.e., diffusion and advection). Based on boundary conditions, the single void dissolution kinetics (SVDK) model allows for the description of how liquid water continuously enters air voids from the surrounding capillary porosity while maintaining thermodynamic equilibrium at the gaseous air - liquid interface. Results are compared to: validated models of simple systems [16,17] (i.e., a gas bubble suspended in an infinite amount of liquid), micro-fluidic studies [13,16,18,19], and to findings of imaging studies [14] which provide a temporal sense of when near-surface air voids of a given size should become completely saturated.

2.0 Literature Review:

The literature review provided for the formulation of the SVDK models is divided into theoretical and experimental sections. Section 2.1 details the seminal theoretical contributions that serve as the physics-based background for the formulation of the SVDK model, beginning with simple systems (i.e., a gas bubble surrounded by an infinite amount of liquid) and increasing in complexity. Additionally, these previous studies are reviewed and used as a means of comparison for how the derived SVDK model advances the state-of-the-art in predicting the long-term saturation rate of air-entrained cementitious materials. Experimental Section 2.2 is

106 organized into two sections. The first section treats specimen-scale phenomena, where the
107 behavior of cementitious materials immersed in a fluid is studied using a variety of experimental
108 techniques. The second section evaluates known void-scale phenomena, where micro-fluidic
109 models are used to provide insight into the phenomenology that would occur within a saturating
110 air void.
111
112 **2.1 – Theoretical Modeling**
113
114 In 1950, Epstein and Plesset [17] developed a model for the evolution over time of a single
115 bubble of gas suspended in a liquid solution. They displayed that by considering mass-balance at
116 the bubble-liquid interface the reduction, growth, or stability of the bubble could be explained. In
117 summary, their derivation was formed around the equivalence of mass-fluxes at the gas-liquid
118 interface where thermodynamic equilibrium must be maintained. Equation 1 displays their final
119 partial differential equation and Table 1 defines its terms. A detailed derivation can be found in
120 [16]. Additionally, multiple forms of the original Epstein-Plesset equations can be obtained when
121 neglecting temporal and surface-tension effects, as shown in [16,20]. From Equation 1, it can be
122 directly seen that the term f, which represents the ratio of the initial dissolved gas concentration
123 in the surrounding infinite fluid to the saturated concentration, will dictate whether the bubble
124 with radius, R, will grow or shrink. With respect to gas bubbles that have surrounding liquids
125 that are not saturated with dissolved gas species (i.e., a value of $f \leq 1$), the model predicts that a
126 gas bubble with initial radius R_0 will completely dissolve due to an internal pressure (given by
127 the Laplace equation) larger than that of the surrounding fluid, which drives the dissolution of
128 gaseous species, understood by Henry's Law, followed by Fickian transport.

$$\frac{dR}{dt} = -Dk_H GT \frac{1 - f + \frac{2M_w\sigma}{\rho GTR}}{1 + \frac{4M_w\sigma}{3\rho GTR}} \left[\frac{1}{R} + \frac{1}{\sqrt{\pi Dt}}\right] \quad (1)$$

Table 1: Definition of terms for the Epstein-Plesset Equation found in Equation 1.

Term:	**Definition (Units):**
R	Bubble radius (m)
T	Time (s)
D	Diffusivity of dissolved gas in surround liquid (m^2/s)
k_H	Henry's constant ($kg/m^3/Pa$)
G	Universal Gas Constant ($m^3.Pa/mol/K$)
T	Temperature (K)
f	Ratio of initial concentration to saturated concentration (-)
M_w	Molar mass of the gas (kg/mol)
σ	Surface tension of the gaseous air – liquid interface (N/m)
ρ	Density of the gas at atmospheric pressure and at the initial temperature (kg/m^3)

Recognizing the applicability of the work in [17] to the long-term saturation of air-entrained cementitious materials in [10], G. Fagerlund proposed three ways in which air voids in cementitious materials could become fully water-saturated. To initiate the dissolution-driven system, Fagerlund assumed that air is trapped in the voids due to the fast imbibition of water into the capillary porosity, characterized by saturation rate S_1 in Figure 1b. Once the gaseous air is trapped in the void it is then compressed to satisfy Laplace effects – given by the size of the void and taking the water in the surrounding capillary pores to be at atmospheric pressure. As a result, the system is a spherical air bubble that is surrounded by a porous paste shell in which the capillary porosity is completely water-saturated, as shown in Figure 2a.

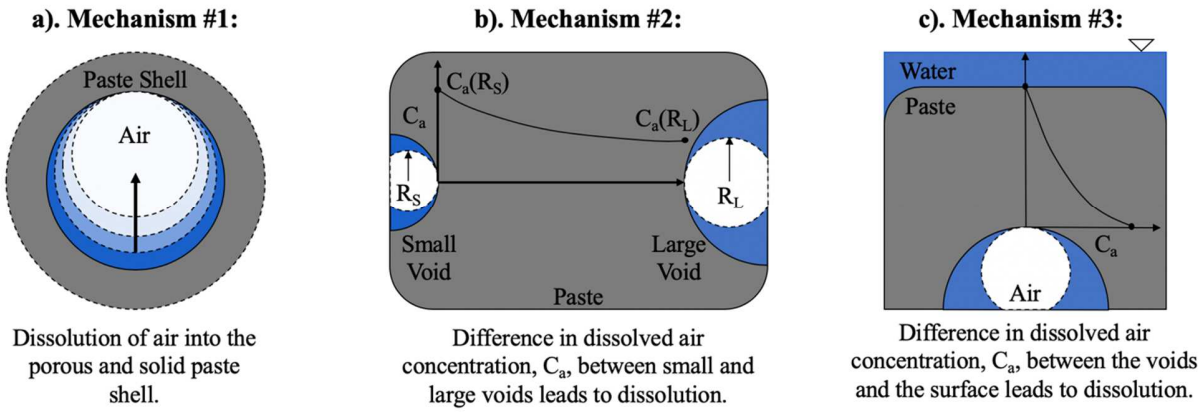

Figure 2 - General mechanisms developed by G. Fagerlund in [10] for how air voids in cement pastes become water-saturated.

Figure 2 shows a general schematic of the models discussed in [10]. The first mechanism suggested that the compressed air will rapidly diffuse into the paste shell if enough water exists in the surrounding capillary pores and that the water is not already saturated with dissolved air. Although this mechanism considers the influence of the initial state of the surrounding capillary water, similar to the term f in Equation 1, it provides no insight into how water enters the void or the time-dependent mass conservation of air and water in the total system. In the second model, shown in Figure 2b, it was suggested that the dissolved air diffuses from small to progressively larger air voids that are nearby, in the spirit of Ostwald ripening. Seeing as how the concentration at the gaseous air-liquid interface is proportional to the inverse of the compressed air bubble size, a concentration gradient of dissolved air would exist between a small and large air void, as shown in Mechanism #2 in Figure 2b, and result in diffusive flow of dissolved air through the water-saturated paste. In the third model, Fagerlund proposed that the saturation of air-entrained cementitious materials depends on the diffusion of the dissolved air within the voids to the surface of the specimen where the concentration of dissolved air is low (assuming that the entire

specimen is immersed in water) – see Mechanism #3 in Figure 2c. In [10], it was additionally displayed how to leverage Mechanism #2 to predict the concurrent filling of a system of air voids and the resulting long-term saturation.

While the work in [10] suggested how air voids could fill with water (i.e., into surrounding porosity, into one another, and to the surface), clear systems of equations, state equations, and boundary conditions were not developed to aid in the fundamental understanding of how air voids become progressively saturated. Moving from the air-void scale to the specimen-scale, numerous efforts have been put forth to explain the fast initial imbibition of a surrounding fluid into cementitious materials, characterized by saturation rate S_1 [21–23]. For the purposes of this work, understanding the slow secondary saturation rate, S_2, is of greater interest. In 2018, Erikkson et al. [24] derived a multi-phase (i.e., solid, liquid, gas) transport and mechanics model to assess the entire saturation curve for air-entrained cementitious materials. Until the idealized specimen arrived at its value of matrix saturation, S_m, the model follows a similar imbibition study found in [23]. Once a representative elementary volume (REV) in the analysis arrives at its matrix saturation S_m, Erikkson et al. assumes that the air voids, which are homogenized within a REV, are filled with compressed air. The compression, as in Fagerlund's work, results in dissolution of air and diffusion of dissolved air through the system and leads to a slow increase of water saturation. The results of the model were found to agree very well with experimental results taken from [25] and suggested that air void systems with more coarse, or broad, air void size distributions saturate more slowly. Additionally, it is important to note that in the work of Erikkson et al. the air voids within an REV are assumed to fill in order of increasing size from [10].

184

185 A multitude of other models exist which aim to predict the time to critical saturation of air-
186 entrained cementitious materials but use experimental data as the basis for which to do so. In
187 [1,4,26] the time to critical saturation is predicted using the value of secondary saturation rate,
188 which is related to the secondary sorptivity, following the work presented in [2]. This method is
189 reliable and can be done to validate that specific concrete or mortar mixtures have a desired
190 minimal service-life. The approach has been adopted by AASHTO [9]. Additionally, based on
191 the assumptions presented and found in [8,10,24], recent efforts have shown how a simple
192 geometric model can be used to predict the evolution in Powers' spacing factor [27,28] between
193 remaining air-filled voids, as more and more air voids become water-saturated [25]. The
194 presented efforts have provided significant insight and advancement with respect to how air-
195 entrained cementitious materials may become increasingly saturated. Nonetheless, numerous
196 gaps remain with respect to governing mechanisms at the air void-scale. The central intention of
197 the SVDK model is to then build on what has been presented in a complementary manner in
198 effort to provide fundamental insight into the water-saturation mechanism for single air voids
199 that occur below the REV scale for models similar to [24].
200

201 **2.2 – Experimental Results**
202

203 **2.2.1 – Specimen Scale Phenomena**
204

205 In 2012, based on a series of highly controlled sorption tests, Li et al. [2] displayed that the
206 secondary saturation rates, S_2, as shown in Figure 3, were approximately equivalent irrespective

of the total air content or the relative humidity at which the mortar specimens were conditioned at prior to conducting ASTM C1585-04 –the standard sorption experiment. This finding served as the justification for a series of models, similar to those found in [1,29], that predicted the time to critical saturation [4,26]. Figure 3 displays the concatenated findings from [2] and shows the similarity in secondary saturation rate S_2 for the respective sorption tests.

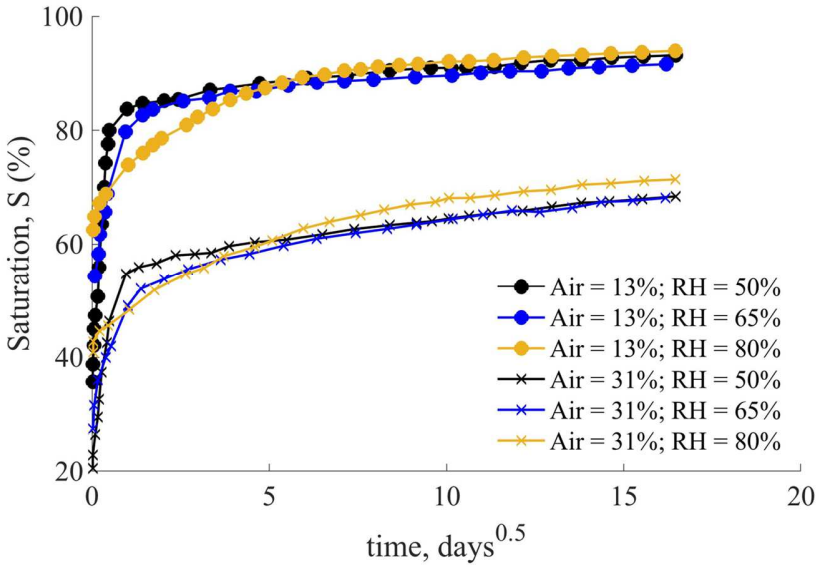

Figure 3 - Concatenated sorption findings from [2] for mortar specimens.

Figure 3 shows that as the relative humidity at which the samples were conditioned prior to conducting sorption testing increases the matrix saturation point (identified as a kink in the saturation versus square-root-of-time curve) is not clearly identifiable. In [30], using neutron radiography, it was displayed that after 12 hours of fluid exposure, air-entrained and non-air-entrained mortars remained below their matrix saturation point from depths of 5mm to 25mm within the specimen. Additionally, at twelve hours of testing it was found that the degree of saturation for all of the specimens were within 5% of the matrix saturation, but not above it at

any point, irrespective of the degree of cement hydration. This finding suggests that the initial saturation regime is exclusively driven by capillary action leading to a saturation state at which the capillary pores are fully liquid-saturated and the air voids remain air-filled. It follows then that for long-term fluid exposure the entrained and entrapped air voids will begin to saturate and make the material progress toward a critically saturated state as shown in Figure 1b.

In 2017, Moradllo and Ley [14] published a series of 8.8μm/voxel μCT results obtained by ponding a potassium iodide solution on top of a cement paste for up to 60 days. Although the paste was not air-entrained, a distribution of spherical voids was found in the hardened specimen and a final analysis was done with respect to their final saturation state. In [14] the cylindrical specimen, size distribution of air voids within the first 6mm of the sample, and which voids became saturated and remained air-filled were displayed. It is important to note that the first 6mm was selected because of a homogeneous concentration in potassium iodide solution within that region (i.e., it was uniformly solution-saturated). Based on their results, it is clear that the air voids, which ranged from 20μm to 500μm in radius, did not fill solely as a function of increasing size. This finding suggests that further efforts are needed to investigate the nature of how air voids become saturated by considering the effect of the relative location of the air voids with respect to one another and their respective distance to a free surface of the specimen.

2.2.2 – Pore Scale Phenomena

As detailed in Section 2.2.1, an experimental investigation capturing the saturation dynamics of a single air void in a cementitious material has yet to be conducted. A great deal of understanding can be gained by studying proxy systems, as idealized in Figure 4a, of trapped air or immobile

bubbles undergoing a temporal process of dissolution, diffusion, and advection that leads to complete liquid saturation. Proxy system 1, idealized from the work conducted in [16,20], provides a simplistic gas-liquid system and was used as a basis to evaluate Epstein and Plesset's original model presented in Section 2.2.1. Proxy systems 2 and 3, in which a gas bubble is resting underneath a flat plate [16,19] or within a well [31] have also been extensively studied experimentally and numerically. Lastly, proxy system 4 provides the closest 2D approximation of how a highly tortuous micro-model can be idealized and used to study the in-place dissolution dynamics of trapped gases [13,18,32]. A series of images capturing the dissolution of a trapped isobutanol bubble within a silica micro-model is shown in Figure 4b.

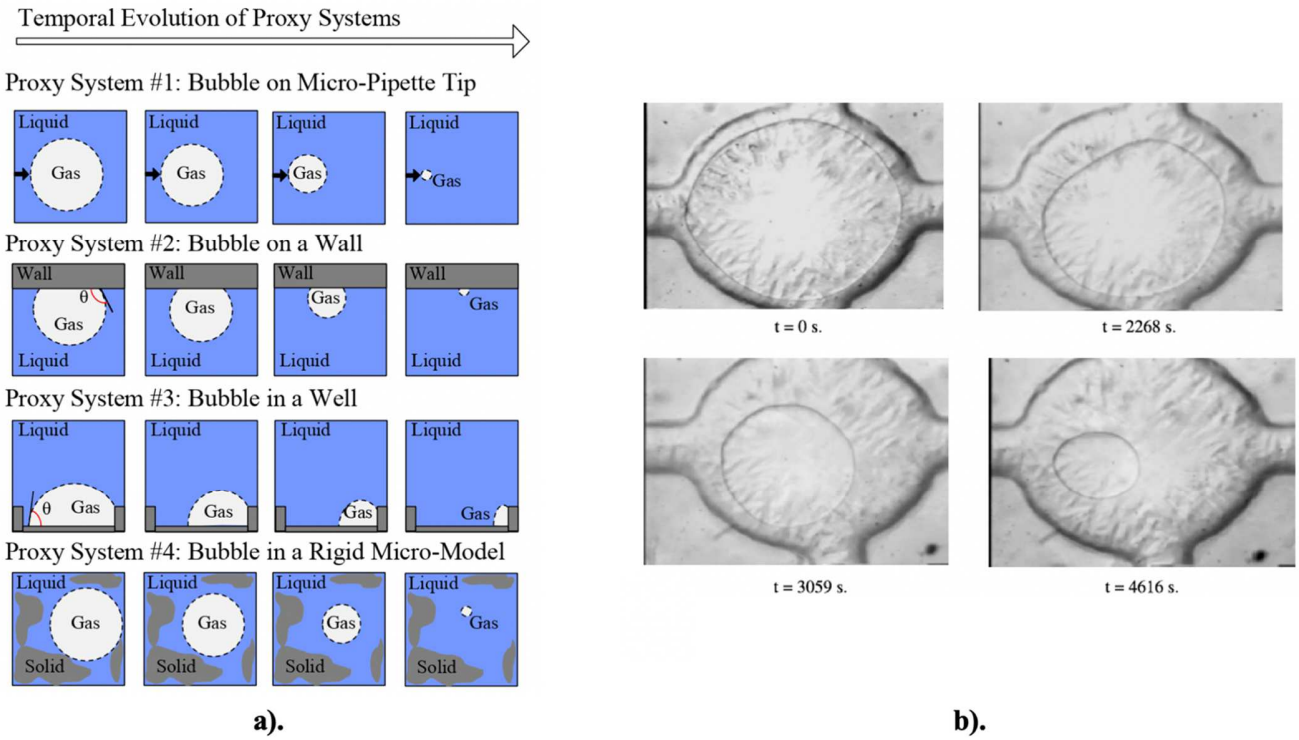

Figure 4 - a). proxy system examples, b). example of dissolution of isobutanol in water as a function of time [13].

In addition to gaining a qualitative understanding of how compressed gases dissolve in gas-saturated liquids, it is well-established [33] that the temporal evolution of droplets and bubbles often follow a universal power-law scaling (i.e., that the radius evolves as a power-law of the difference between the time-to-full-dissolution and the actual time, see Figure 5a). As displayed in [33,34], for steady-state and diffusion-controlled conditions, the radius and time of liquid droplets have such ½ power law relationship. Referring to Equation 1, when the temporal term and surface tension are neglected and f is unity, it can be shown that the size reduction of a gas bubble surrounded by an infinite amount of fluid follows such a ½ power law. However, when these assumptions are not made, the exponent of the power-law relationship can significantly vary. Figure 5a displays a concatenated group of experiments representing proxy systems 1 to 4, for which time-to-full-dissolution was fit so that power-law relationships were obtained. Based on these analyses, it can be seen that the determined exponents of the power-law relationship, found in the legend and denoted by C, range from 0.33 to 0.86. Figure 5b displays the determined exponents of the power-laws for solutions to the Epstein-Plesset equation for various values of f and surface tension. From Figure 5b it can be seen that the exponent of the power-law ranges from 0.36 to 0.52 for the Epstein-Plesset model. For proxy systems 1-3, the exponents found for the radius-time relationship agree well. The exponents found for proxy system 4 are generally higher, which we attribute to the influence of dealing with a non-3D system.

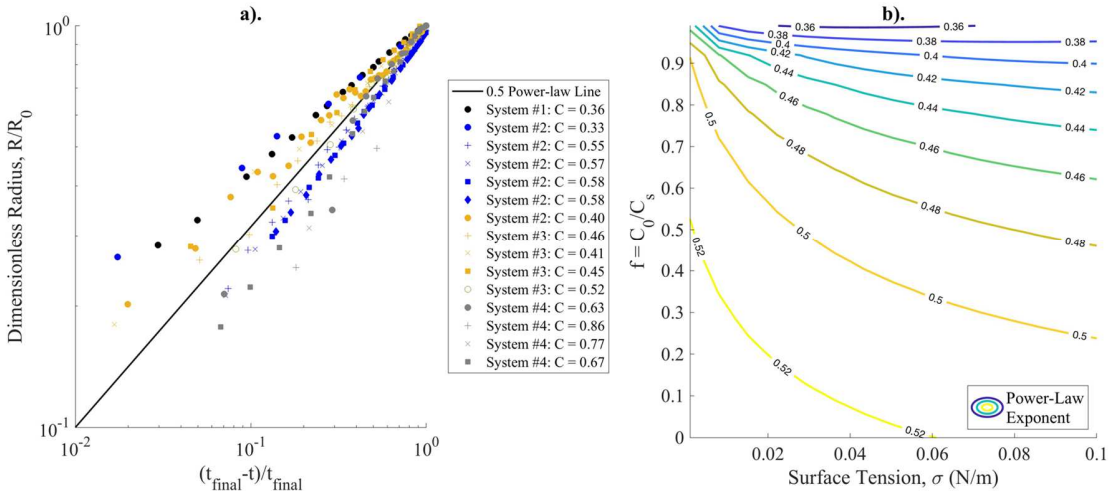

Figure 5: a). Outcomes of fit-power laws to a large class of proxy-systems [13,16,18,19], b). Exponent of power-law fits for solutions to the Epstein-Plesset model for initial bubble radius of 15μm.

It is also important to note that the Epstein-Plesset model has been experimentally validated. In 2004 and 2006, Duncan and Needham [16,35] displayed the ability of the model presented in [17] to predict the size reduction of gas bubbles placed on the tip of a micro-pipette or against a flat, impermeable wall. Original results for the validation can be found in [16]. Additionally, the exponent of the power-law relationship between the radius and time history was found to be 0.37 and 0.33, for the bubble on the micro-pipette and resting on a flat wall, respectively. Based on the reduction in exponent, the presence of the wall causes the radius of the bubble to reduce in size slower than if it was suspended in an infinite liquid, which is a state of isotropic diffusion. Although the presented proxy systems are significantly more ideal than what can be expected in air-entrained cementitious materials, their analysis still provides profound insight into the

294 qualitative and quantitative nature of how trapped gases reduce in size as a function of their
295 surroundings.
296
297 **3.0 Void-Scale Model: Single Void Dissolution Kinetics (SVDK)**
298
299 By considering the following pore-scale and specimen-scale findings presented in Section 2.2 in
300 a consistent framework, it is clear that many open questions still exist. Regarding the long-term
301 saturation phenomenon, a central question that remains is: by what physics-based mechanism do
302 the spherical air voids become water-, or liquid-, saturated? Section 3 is oriented around deriving
303 a model which advances current answers to this void-scale question. Pending an improved
304 understanding of the pore-scale phenomenology, it is also of interest to see how its behavior
305 compares to the Epstein-Plesset model detailed in Section 2.2.1 and the proxy systems displayed
306 in Section 2.2.2.
307
308 As displayed in Figure 1a, the macro-system of interest is a porous cementitious paste in which
309 spherical air voids can be found - analogous to the μCT specimen assessed in [14]. For the
310 purposes of the ensuing section, the macro-system is considered to be fully immersed in water
311 and when a spherical region is taken around a single air void, the capillary pores connect the air
312 voids to the surface of the specimen and one another. Figure 1b, building on Figure 1a, then
313 shows that the following work is interested in understanding how the secondary saturation rate
314 occurs due to the saturation of single spherical air voids. The pore-scale image below the
315 saturation curve in Figure 1b qualitatively displays how compressed air is expected to behave
316 once the void-scale system has reached the matrix saturation, S_m. The evolution of the air-liquid

317 interface was informed by experimental outcomes that captured the dissolution of trapped gas in
318 infinite liquid or micro-models - displayed in Figure 4b – which serve as proxy systems of study
319 for air-entrained cementitious materials.
320
321 From now on, an individual air void surrounded by a spherical shell of saturated cement paste is
322 considered. The modeling of the progressive saturation of this air void will lead to what we call
323 the single-void dissolution kinetics (SVDK) model. Within Sections 3.1 to 3.3 the single-void
324 dissolution kinetics (SVDK) model is derived to provide insight into how air voids in
325 cementitious materials, and other analogous porous media, become saturated over time. Section
326 3.1 defines a system which can be mathematically evaluated and how the gaseous air-liquid
327 interface can be represented at any level of air-void saturation. Within this section, specific
328 attention is given to how the system can be initiated at time $t = 0$ and the implications that the
329 initial geometry will have on the long-term dissolution kinetics. Section 3.2 contains the model
330 formulation and presents assumptions. Detail is given to how the assumptions can be expected to
331 influence the model outcomes with corresponding justifications. Section 3.3 provides the results
332 and an extended discussion of the model outcomes. Lastly, Section 4.0 contains conclusions,
333 implications of the model outcomes for the broader field of cementitious-material durability
334 research, and opportunities for future work.
335
336 **3.1 System Definition and Initial Geometry**
337
338 The initial step to developing and understanding the dissolution of compressed gas within a
339 single air void, and its resulting saturation, is idealizing the system, and in particular its

340 geometry, so that it can be mathematically represented. Figure 6 shows the bilinear saturation
341 regime common for air-entrained cementitious materials where saturation rate S_2 characterizes
342 the dissolution-driven regime. As detailed, it is of interest to understand this long-term saturation
343 phenomenon at the void-scale as the matrix saturation represents the saturation state at which all
344 of the capillary pores are filled with liquid water and the larger spherical voids contain trapped
345 gaseous air.
346
347 The contact angle of the liquid at the surface of the air void is denoted θ and is assumed to
348 remain constant over time. From the fluid-immersed macro-scale system, a spherical region of
349 interest is defined around a single air void. The air bubble in the air void is considered to rest at
350 the top of the air void because of gravity. Equation 2 displays the mathematical representation of
351 the volume of the gaseous air region, V_g, trapped within the spherical void, which is the volume
352 of intersection of two spheres of radius R_v (which is the radius of the air void) and R_{gl} (which is
353 the radius of curvature of the air-liquid interface) [36]. Following this equation, for a given
354 contact angle θ of the liquid-air-solid interface, there is a unique relationship between the liquid
355 saturation of the air void with radius R_V and the radius of the gas-liquid interface, R_{gl} (see Figure
356 6). It is important to note that because V_g will evolve as a function of time during the saturation
357 process, the radius R_{gl} will also vary temporally, which governs the Laplace pressure in the air
358 bubble. Lastly, d, the lineal distance between the centers of the spheres of radius R_v and $R_{gl}(t)$ is
359 written in Equation 3. The volume of the liquid can then be directly calculated as the difference
360 in the volume of the spherical void, given by $(4/3)\pi(R_v)^3$, and V_g.
361

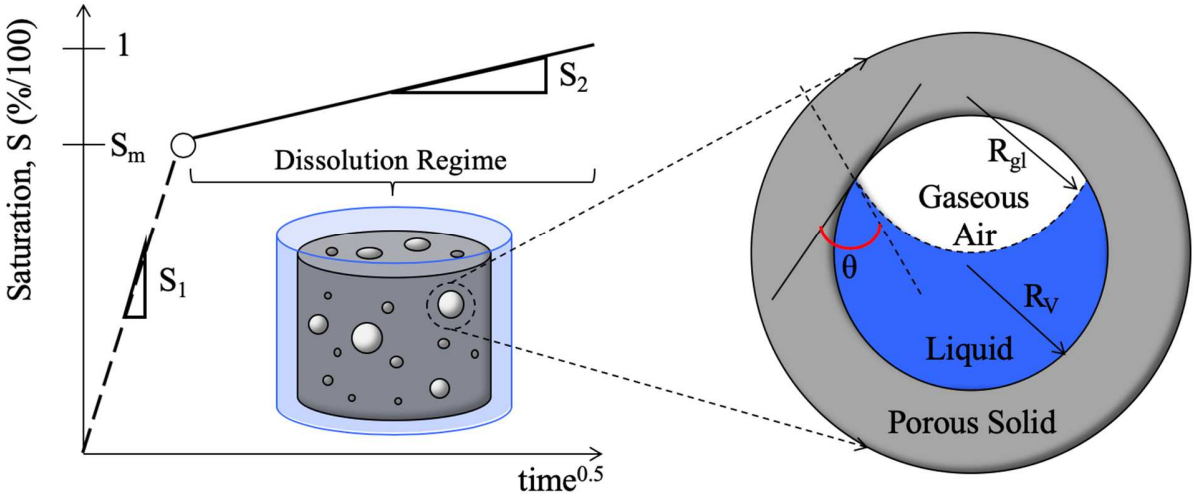

Figure 6: Spherical void-shell system and representation of the gas liquid interface which, for a given contact angle, θ, can be parametrized by the radius of the interface, R_{gl}.

$$V_g\left(R_V, R_{gl}(t), \theta, d(t)\right) = \frac{\pi}{12d}\left(R_v + R_{gl}(t) - d(t)\right)^2\left(d(t)^2 + 2dR_{gl}(t) - 3R_{gl}(t)^2 + 2dR_v + 6R_{gl}(t)R_v - 3R_v^2\right) \quad (2)$$

$$d\left(R_V, R_{gl}(t), \theta\right) = \left(R_v^2 + R_{gl}(t)^2 - 2R_V R_{gl}(t)\cos\theta\right)^{1/2} \quad (3)$$

The porous solid shell surrounding the spherical void shown in Figure 6 is considered to be saturated at all times and the capillary pores are no longer displayed since they are orders of magnitude smaller than the voids [15]. The stipulation that the capillary pores are always completely liquid-saturated implies that saturation states below S_m are not considered in the SVDK model. Because the initial imbibition of liquid through the surrounding capillary pores is assumed to be complete, it is uncertain if all of the original air in the void remains present or if more, or less, air is present than was present in the void's volume before immersion, when air

375 was still at atmospheric pressure. For example, it is possible that, during the imbibition process,
376 some of the air initially present in the capillary pores was forced into the spherical voids.
377 Conversely, it is also possible that, during the imbibition process, part of the air initially in the air
378 void could have escaped outward. Consequently, in our study, we consider a large domain of
379 initial gaseous air mass trapped in the air void.
380
381 To define the initial geometry of the system at time t = 0 (corresponding to the moment when all
382 capillary porosity is saturated), for a given contact angle θ of the liquid on the solid, two
383 parameters of the void-scale system need to be defined: the mass of the trapped gas in the void,
384 and the initial pressure at time t = 0 of the liquid, P_l, or of the gas, P_g. We introduce a normalized
385 trapped mass of gas, m_t, where the mass used for normalization is that of air (considered as an
386 ideal gas) at atmospheric pressure filling the spherical air void. The mass of gas trapped in the
387 void, m_g, can then be calculated by Equation 4. Definitions for other terms presented in Equation
388 4 can be found in Table 1. To determine the initial geometry for a given normalized mass,
389 $m_g(t=0)$, of trapped air, Equation 5 is numerically solved where $R_{gl}(t=0)$ is the only unknown, as
390 θ is prescribed. Additionally, as is done in [10], we assume that at time t = 0 the liquid pressure,
391 P_l, is at atmospheric pressure, P_{atm}, so the pressure of the trapped gas (whose volume is given by
392 $V_g\left(R_V, R_{gl}(t=0), \theta, d\right)$), is P_{atm} plus the Laplace pressure - which is inversely proportional to
393 the radius of the gas-liquid interface, $R_{gl}(t=0)$. It is important to note that other assumptions
394 could have been made: for instance, we could have assumed that the pressure of the trapped gas
395 at time t = 0 is equal to P_{atm}. This assumption on initial pressure, and its implications on the
396 dissolution dynamics of the trapped gas, will be discussed within Section 3.4.
397

398

$$m_g(t) = m_t \frac{P_{atm} \frac{4}{3} \pi R_v^3 M_w}{GT} \quad (4)$$

399

$$m_g(t=0) - \frac{\left(P_{atm} + \frac{2\sigma}{R_{gl}(t=0)}\right) V_g\left(R_V, R_{gl}(t=0), \theta, d\right) M_w}{GT} = 0 \quad (5)$$

400

401

402 Figure 7 displays a contour plot of initial normalized masses, m_t, of trapped gas, as a function of
403 the contact angle, θ, and of the radius of curvature, $R_{gl}(t=0)$, of the gas-liquid interface. Figure
404 7's contour plot can be understood as a 'look-up' chart for initial system geometries based on the
405 previously presented assumptions. Next to the contour plot are a series of 6 different initial
406 geometries, identified by letters A - F. Figure 7 shows that, for a given non-zero contact angle, θ,
407 if the trapped mass of air is larger than a critical value, there exists no solution to Equations 4
408 and 5: such states cannot exist physically under the assumption of liquid water at atmospheric
409 pressure. For instance, for $\theta > 32°$ and a normalized trapped mass, m_t, of 1, Figure 7 shows that
410 there are no initial geometries.

411

412 No contour plot can be drawn for trapped masses greater than the value given by Equation 6,
413 which, in the present case of spherical voids with a radius of 10µm, corresponds to a normalized
414 trapped mass of 1.13. If a larger mass of air is initially trapped in the air voids, i.e. if, at time t =
415 0, air in the capillaries pores was pushed into the spherical void during the fast liquid water
416 imbibition process, the air void would be completely filled with gaseous air and the gas-liquid
417 interface would be located inside the capillary pores rather than inside the air void. In such case,
418 the geometry of the gas-liquid interface would no longer be governed by Equations 4 and 5. It is

possible that air would dissolve and diffuse until the pressure of the air (which would still occupy the full air void) reaches atmospheric pressure, at which point thermodynamic equilibrium would be reached and the radius of curvature of the gas-liquid interface, still located in the capillary pores, would be infinite: the air void would remain full of air and would never fill with liquid, even when left indefinitely under water.

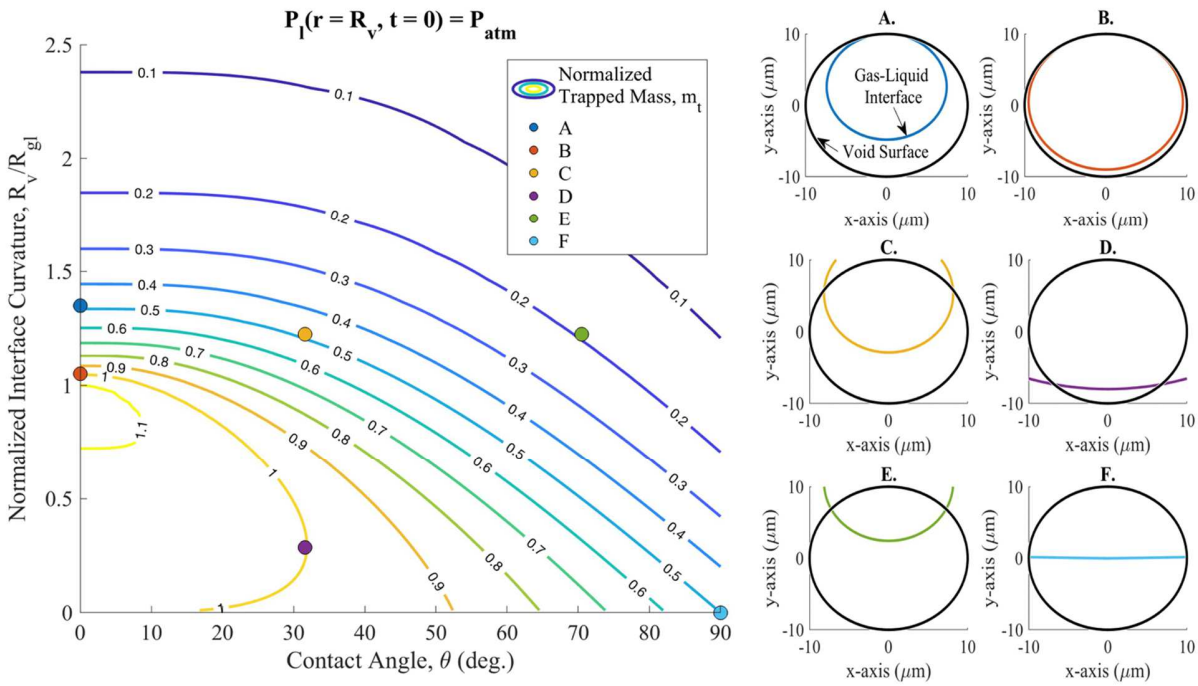

Figure 7: Contour plot of normalized mass of air initially trapped, as a function of contact angle, θ, and initial radius of the gas-liquid interface, $R_{gl}(t=0)$ with associated visualization of corresponding initial system geometries. All calculations are made for R_v = 10μm.

$$m_t^{max} = \frac{P_{atm} + \frac{2\sigma}{R_v}}{P_{atm}} \quad (6)$$

Figure 7 also shows that there exist combinations of contact angle θ and normalized initial trapped mass m_t for which more than one potential initial geometry exists (for example for $m_t = 1$ and θ = 25 degrees, for which there are two potential values of $R_{gl}(t=0)$). In this case, for subsequent calculations, we considered that the system adopted the configuration with the lower free energy, where the free energy, E_{sum}, of an initial geometry is calculated based on Equation 7. Note that, if the other configuration (with high free energy) is adopted as the initial configuration, the model would predict that air would dissolve until the radius of curvature of the gas-liquid interface would be infinite. Starting from this other configuration, one would hence find out that the air void would remain at least partially filled with air and would never become full saturated with a liquid, even when left indefinitely under water. Equations 8 through 10 display how the gas, E_g, surface, E_{surf}, and bulk liquid, E_{vol}, free energies are respectively calculated, where in Equation 9 σ is the gaseous air – liquid interfacial surface tension, γ_{gas}^{solid} is the gaseous air – solid paste interfacial surface tension, and γ_{liquid}^{solid} is the liquid – solid paste surface tension.

$$E_{sum}\big(R_{gl}(t=0),\theta\big) = E_{gas}\Big(R_{gl}(t=0)\Big) + E_{surf}\big(R_{gl}(t=0),\theta\big) + E_{vol}\big(R_{gl}(t=0),\theta\big) \quad (7)$$

$$E_{gas}\Big(R_{gl}(t=0)\Big) = \frac{4\pi}{3} R_v^3 P_{atm} ln\left(1 + \frac{2\sigma}{R_{gl}(t=0) P_{atm}}\right) \quad (8)$$

$$
\begin{aligned}
E_{surf}\left(R_{gl}(t=0),\theta,d\right) &= E_{gas}^{liquid}+E_{gas}^{solid}+E_{liquid}^{solid} \\
&= 2\pi\sigma R_{gl}(t=0)^2\left(1-cos\left(\theta\sin^{-1}\left(\frac{R_v}{d}\right)\right)\right) \\
&+ 2\pi\gamma_{gas}^{solid}R_v^2\left(1-cos\left(\theta\sin^{-1}\left(\frac{R_{gl}(t=0)}{d}\right)\right)\right) \\
&+ 2\pi\gamma_{liquid}^{solid}R_v^2 cos\left(\theta\sin^{-1}\left(\frac{R_{gl}(t=0)}{d}\right)\right)
\end{aligned} \tag{9}
$$

$$
E_{vol}\left(R_{gl}(t=0),\theta\right) = P_{atm}V_g\left(R_V,R_{gl}(t),\theta,d\right) \tag{10}
$$

Finally, it is important to note that due to the fact that the capillary pores are orders of magnitude smaller than the spherical voids, the trapped gaseous air cannot 'escape' under the form of tiny gas bubbles by rising through the saturated capillary porosity, as can be directed evaluated from a calculation of the breakthrough pressure presented in [37]. The only way for the air to escape outward and for the air void to become saturated is through dissolution and diffusion, which are modeled in the next section.

3.2 Model Formulation and Assumptions

For the purpose of modeling the saturation of the void-shell system presented in Figure 6, it is of principal interest to understand the transport of the liquid water within the porous solid shell into the spherical void and the resulting dissolution dynamics of the trapped gas. As detailed in the review of the model presented by Epstein and Plesset, the liquid also contains dissolved gas which fluxes into the fluid to maintain thermodynamic equilibrium at the gas-liquid interface. By writing the continuity of the diffusive mass fluxes of dissolved air in the liquid at the surface of the air void (i.e., within the void and within the saturated porous solid shell), we show with Equation 11 that the gradient of concentration of dissolved gas (this concentration is denoted as

468 C_g) is orders of magnitude smaller in the liquid in the air void than in the porous shell. Indeed,
469 the diffusivity of air in liquid water, D_g^l, has a value of 10^{-8} cm^2/s [16] whereas the diffusivity of
470 dissolved air in saturated hydrated cement paste, D_g^s, is on the order from 10^{-10} to 10^{-13} cm^2/s
471 [38]. Based on this result, we assume that the concentration of dissolved gas, C_g, is homogeneous
472 in the liquid within the air void and must satisfy thermodynamic equilibrium of the gas-liquid
473 interface. Thanks to this assumption, the concentration of dissolved gas, C_g, is the same
474 everywhere around the surface of the spherical void (i.e. at r = R_V).
475

$$\left.\frac{\partial C_g}{\partial r}\right|_{r=R_V^-} \Big/ \left.\frac{\partial C_g}{\partial r}\right|_{r=R_V^+} = \frac{D_g^s}{D_g^l} \ll 1 \qquad (11)$$

476
477 As a result, the 3D system of interest can be simplified into a 1D system (see Figure 8), where
478 the concentration of dissolved gas in the liquid saturated porous shell will be evaluated as a
479 function of time in the shell (of thickness L), i.e. from r = R_V to r = R_V + L. As a consequence of
480 the evolution of the size and mass of the trapped gaseous air within the spherical void during the
481 saturation process, the concentration C_g of dissolved gas at the surface of the air void (i.e. at
482 r=R_V) will need to be properly integrated into the system of equations to be solved.
483
484

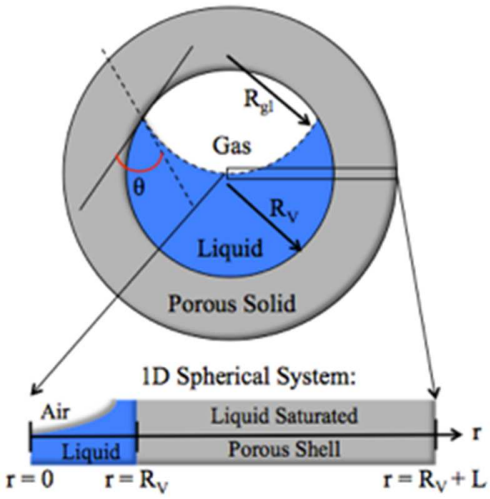

485

486 **Figure 8:** Simplification of problem to 1D.

487

488 By conserving all phases present in the porous shell (i.e. liquid water and dissolved gas), the
489 mass conservation of liquid water, l, and dissolved gaseous air, g, can be written by the
490 advection-diffusion equation following [39]. Equation 12 shows the advection-diffusion equation
491 for the liquid, l, where ρ_l is the liquid density, κ is the intrinsic permeability of the porous solid
492 shell, φ_0 is the porosity of the shell, η is the dynamic viscosity of the liquid, and P_l is the liquid
493 pressure. Equation 13 displays the advection-diffusion equation for the dissolved air within the
494 liquid in the porous solid shell where C_g is the concentration of dissolved gas in the liquid. In
495 Equations 12 and 13, the material parameters (i.e., κ, φ_0, η, and D_g^s, whose meaning is given in
496 Table 3) in the porous shell are taken as homogeneous in space and constant over time.
497 Additionally, it is assumed that the liquid flow is incompressible and that the density of the
498 liquid, ρ_l, is not a function of the dissolved gas concentration [40], implying that this density, ρ_l,
499 is assumed constant. As shown in Equation 14, the incompressible flow condition of the liquid in
500 the porous solid shell results in $r^2 \partial P_l / \partial r$ being constant from r = R_V to r = R_V + L. The final

governing equation for the mass transport of the dissolved gas in the liquid saturated porous shell is written as Equation 15, where $r^2 \partial P_l / \partial r$ is homogeneous in space, but varies over time.

$$\frac{\partial \rho_l}{\partial t} - \rho_l \frac{\kappa}{\varphi_0 \eta} \frac{1}{r^2} \frac{\partial}{\partial r}\left(r^2 \frac{\partial P_l}{\partial r}\right) = 0 \tag{12}$$

$$\frac{\partial C_g}{\partial t} - \frac{\kappa}{\varphi_0 \eta} \frac{1}{r^2} \frac{\partial}{\partial r}\left(r^2 \frac{\partial P_L}{\partial r} C_g\right) - \frac{D_g^s}{\varphi_0} \frac{1}{r^2} \frac{\partial}{\partial r}\left(r^2 \frac{\partial C_g}{\partial r}\right) = 0 \tag{13}$$

$$r^2 \frac{\partial P_l}{\partial r} = cons = \left(P_l(r = R_v + L, t) - P_l(r = R_v, t)\right) \frac{1}{\frac{1}{R_v} - \frac{1}{R_v + L}} \tag{14}$$

$$\frac{\partial C_g}{\partial t} - \frac{\kappa R_v (R_v + L)}{\varphi_0 \eta} \frac{\left(P_l(r = R_v + L) - P_l(r = R_v, t)\right)}{r^2 L} \frac{\partial C_g}{\partial r} - \frac{D_g^s}{\varphi_0} \frac{1}{r^2} \frac{\partial}{\partial r}\left(r^2 \frac{\partial C_g}{\partial r}\right) = 0 \tag{15}$$

To solve Equation 15, the boundary conditions for the liquid pressure, P_l, and dissolved gas concentration, C_g, must be known. At $r = R_V + L$, the liquid pressure is taken equal to the atmospheric pressure, P_{atm}, and the concentration in dissolved gas is considered to be equal to that in water in equilibrium with air at atmospheric pressure, such that, with Henry's law, the concentration of dissolved gas, C_g, at $r = R_V + L$, is given by the product, $k_H P_{atm}$ [10,17], where k_H is Henry's constant for air. To understand how C_g and P_l vary at $r = R_V$, they are written as a function of the mass of the gas, $m_g(t)$, and the mass of the liquid, $m_l(t)$, within the spherical void. To do so, it is assumed that the mass of dissolved gas in the liquid within the spherical void is negligible based upon [40] - implying that the mass of gas is exclusively given by the trapped volume defined by $R_{gl}(t)$, which, for a given contact angle θ, is a function of $m_l(t)$. Based on this assumption, the concentration of the dissolved gas at $r = R_v$ can be expressed for all times by

519 combining Henry's Law and the Ideal Gas law as displayed in Equation 16. Additionally, the
520 liquid pressure at r = R_V can also be expressed, as shown in Equation 17, by combining Henry's
521 law, the ideal gas law, and Laplace equation.
522

$$C_g(r = R_v, t) = C_g\big(m_g(t), m_l(t)\big) = \frac{k_H m_g(t) GT}{M_w\left(\frac{4\pi}{3}R_v^3 - \frac{m_l(t)}{\rho_l}\right)} \tag{16}$$

523

$$P_l(r = R_v, t) = P_l\big(m_g(t), m_l(t)\big) = \frac{m_g(t) GT}{M_w\left(\frac{4\pi}{3}R_v^3 - \frac{m_l(t)}{\rho_l}\right)} - \frac{2\sigma}{R_{gl}(m_l(t))} \tag{17}$$

524

525 To have a solvable system of equations, $m_g(t)$ and $m_l(t)$, the masses of gaseous air and of liquid
526 water within the spherical void, can be determined by evaluating the respective mass fluxes
527 through the spherical void surface. Equation 18 calculates the rate of change of the mass of
528 gaseous air in the spherical void by summing the advective and diffusive mass fluxes through the
529 spherical void surface. Equation 19 is written in a similar form to calculate the rate of change of
530 liquid in the spherical void. In Equation 19, the term, C_l, denotes the concentration of liquid in
531 the pore solution and thus is equal to the difference between the liquid density, ρ_l, and the
532 dissolved gas concentration, C_g, at r = R_v at any time. When replacing C_l with this difference,
533 Equation 19 becomes Equation 20.
534

$$\frac{\partial m_g}{\partial t} = 4\pi R_v^2\left(D_g^s \frac{\partial C_g}{\partial r}\bigg|_{r=R_V^+} + \frac{\kappa}{\eta} C_g \frac{\partial P_l}{\partial r}\bigg|_{r=R_V^+}\right) \tag{18}$$

535

$$\frac{\partial m_l}{\partial t} = 4\pi R_v^2\left(D_g^s \frac{\partial C_l}{\partial r}\bigg|_{r=R_V^+} + \frac{\kappa}{\eta} C_l \frac{\partial P_l}{\partial r}\bigg|_{r=R_V^+}\right) \tag{19}$$

536

$$\frac{\partial m_l}{\partial t} = 4\pi R_v^2 \left(-D_g^S \frac{\partial C_g}{\partial r}\bigg|_{r=R_V^+} + \frac{\kappa}{\eta}(\rho_l - C_g)\frac{\partial P_l}{\partial r}\bigg|_{r=R_V^+} \right) \quad (20)$$

537

538 As a result, Equations 15 to 17, 19, and 20 represent a complete system of equations. This
539 system can then be solved, given the initial condition m_t, and the previously defined boundary
540 conditions for C_g and P_l at $r = R_V + L$, thus making it possible to understand the dissolution
541 kinetics of trapped gaseous air due to coupled-transport of fluid and dissolved gas by advection
542 and diffusion. It is important to note that the gradients of liquid pressure P_l in equations 18 and
543 20 also appear in Equation 14. It can be seen that if the liquid pressure within the spherical void
544 is imposed to be equal to the atmospheric pressure at all times at the surface of the air void then a
545 purely diffusive-driven dissolution model for the trapped gaseous air is obtained.

546

547 **3.3 SVDK Model Results and Discussion**

548

549 **3.3.1 Comparison with Epstein-Plesset Model**

550

551 As motivated in the review and detailed in the SVDK model formulation, understanding how the
552 air voids become liquid filled and how various modes of mass transport (i.e., diffusion and
553 advection) influence the dissolution dynamics and resulting saturation of the spherical void is of
554 central importance to fundamentally understanding the long-term saturation of air-entrained
555 cementitious materials and other materials with similar multi-scale pore structures. Prior to
556 displaying and discussing these phenomena for cementitious materials and other analogous
557 porous media, it is first of interest to evaluate the SVDK model in the context of the Epstein-
558 Plesset model. Although the formulations are notably different and departures can be expected

559 due to the presented assumptions, if the porous solid shell surrounding the spherical air void is
560 treated as liquid water and the initial amount of trapped air, m_t, is equal to 1 and the contact
561 angle, θ, is zero, then systems at time t = 0 are analogous.
562
563 Figure 9a displays results for the Epstein-Plesset model and the SVDK model when the porous
564 solid is treated as liquid water and when advection is neglected (i.e., the liquid pressure at $r = R_V$
565 is considered equal to P_{atm} for all times), for an initial air bubble with a radius of 15µm. Table 2
566 displays the necessary input values for the respective models. It can clearly be seen that the
567 initial linear portion of the two models agree well in terms of rate. Once the radius of the trapped
568 gas reduced below 12µm, the models and experimental behavior of the trapped air becomes
569 increasingly non-linear. Ultimately, because the SVDK model assumes that the concentration of
570 the dissolved gaseous air in the liquid is homogeneous within a sphere of radius of 15µm (which
571 is a reasonable assumption for tortuous porous media as shown in Equation 11, but not a
572 reasonable assumption for a bubble surrounded solely by liquid water) and satisfies
573 thermodynamic equilibrium of the liquid-air interface, the SVDK model logically predicts a
574 collapse of the air bubble being faster than that given by the Epstein-Plesset model. Otherwise, in
575 terms of comparison, the SVDK model agrees very well with the Epstein-Plesset model in terms
576 of order of magnitude but eventually predicts –as could be expected– a smaller (by about 22%)
577 time to full dissolution. Figure 9b displays the evolution of the air-liquid interface with the
578 SVDK model, which is qualitatively very comparable to Figure 4b.
579
580

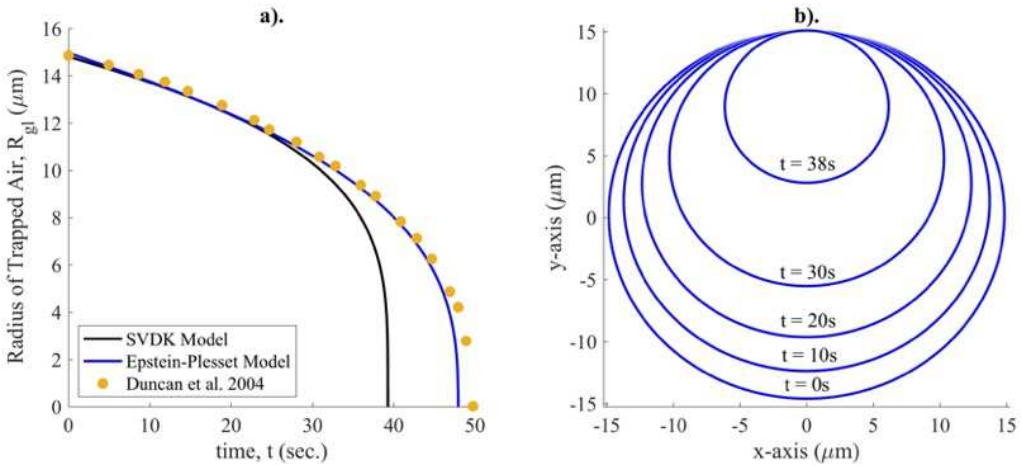

Figure 9: a). comparison of SVDK model to Epstein-Plesset solution (i.e., Equation 3-1) and experimental data of Duncan 2004 [16], b). evolution of air-liquid interface as predicted by the SVDK model.

Table 2: Required inputs for SVDK model and Equation 3-1 to results displayed in Figure 13a/b.

Symbol	Definition	Value
T	Temperature	295.15 K
M_w	Molar mass of air	28.97 g/mol
G	Universal Gas Constant	m^3*Pa/(mol*K)
f	Ratio of initial concentration to saturated concentration	1
σ	Air-water surface tension with a surfactant used in [16]	40 mN/m [16]
D^1	Diffusivity of air in water	$1.8*10^{-9}$ m^2/s [16]
ρ	Density of air	1.225 kg/m^3
k_H	Henry's law of for air in water	$1.9*10^{-7}$ $kg/(m^3*Pa)$ [16]

1. In this evaluation D_g^s is equivalent to the D defined and given in this table.

3.3.2 Discussion of the Role of Advection

For the purposes of the remaining results section, the findings of the SVDK model will be reported for material values expected for well-hydrated cement pastes and the kinetics of the

593 trapped air geometry are compared to behavior seen for the proxy systems presented in Section
594 2.2.2. Additionally, the system is assumed to be at room temperature. Table 3 displays specific
595 values, or ranges of values, that are taken for the SVDK model inputs that are not held constant
596 or already given in Table 2. In terms of organization, Figures 10 and 11 display the influence of
597 advection and the order of magnitude of the intrinsic permeability, κ, while the diffusivity of the
598 dissolved gas in the liquid saturated porous shell is taken as the mean value of the range
599 presented Table 3 (i.e., a value of $5x10^{-12}$ m^2/s). The size of the spherical air void is also taken as
600 $R_V = 10\mu m$, representing the absolute lower bound for entrained air voids in cementitious
601 materials [15] and L is set to 1mm.
602
603 **Table 3:** SVDK model inputs for cementitious material systems.

Symbol	Definition	Value
D_g^s	Diffusivity of dissolved air in saturated hydrated cement paste	$10^{-10} – 10^{-13}$ m^2/s [41]
κ	Intrinsic permeability of hydrated cement paste	10^{-18} to 10^{-22} m^2 [42]
η	Dynamic viscosity of water	$8.9x10^{-4}$ Pa*s
φ_0	Porosity of cement paste	0.20 – 0.30 (-) [42]
σ	Air-water surface tension	70 mN/m [16]
ρ_l	Density of water	997 kg/m^3

604
605 More specifically, in Figure 10, the influence of the liquid pressure, P_l, boundary condition is
606 evaluated and κ is set to 10^{-19} m^2. As detailed in the formulation, the influence of advection on
607 the transport of the dissolved air can be not solved for when P_l is required to be equivalent to P_{atm}
608 at $r = R_V$ and within the liquid in the void. Figure 10a displays the change in radius of the
609 trapped air when $m_t = 1$ and $\theta = 0$. The findings in Figure 10a display that when advection is
610 considered the total time to dissolution increases by approximately 15%. Upon reviewing Figure

10b, which displays the evolution in the liquid pressure at $r = R_V$, it can be seen that when advection is considered, the liquid pressure at the surface of the air void drops below the atmospheric pressure. The reduction in the liquid pressure at $r = R_V$ results in a pressure gradient that pulls liquid into the air void and slows the diffusion of the dissolved gas through the porous solid shell (because it slows the increase of pressure in the gas bubble), causing a longer time to full dissolution of the trapped air.

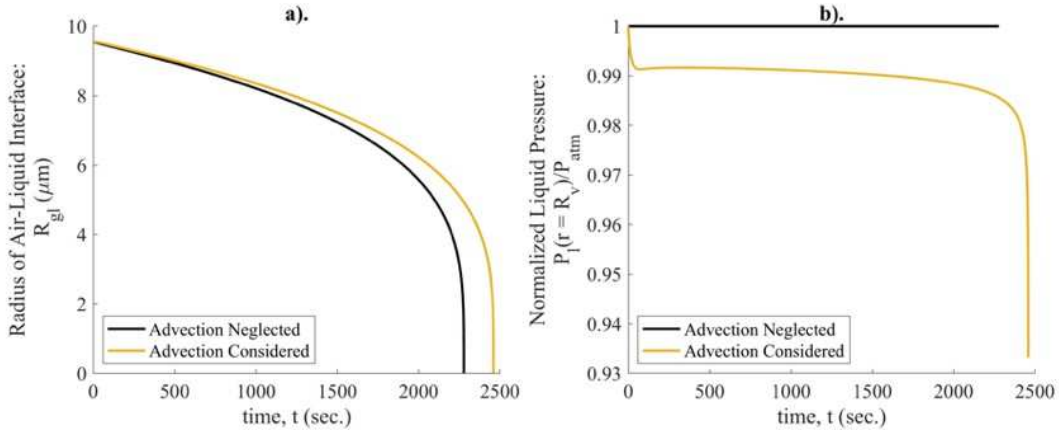

Figure 10: Influence of advection on time to complete dissolution displayed by a). radius of air-liquid interface. b). Evolution of liquid pressure at $r = R_V$ for when advection is neglected (i.e., not solved for) and considered, respectively. Model inputs: $m_t = 1$, $\theta = 0$, $D_g^s = 5x10^{-12}$ m^2/s, $\kappa = 10^{-20}$ m^2.

Figure 11a displays the influence of the value of intrinsic permeability, κ, on the dissolution kinetics of the same trapped air. Interestingly, as κ approaches the maximum usual value for cementitious materials as shown in Table 3, it begins to approximate the solution in which advection is neglected (i.e., not solved for) whereas when κ approaches the minimum usual value

for cementitious materials the time to dissolution significantly increases. This phenomenon can be understood by considering the implications of the results presented in Figure 11b. When the value of κ is large, the pressure gradient quickly reduces because the liquid can quickly flow into the spherical void. When κ is high, a pressure gradient, as seen for smaller values of κ, between r = R_V and r = R_V+L cannot be sustained and is mostly diffusion-driven. This finding is in line with the drying asymptotics of quite permeable porous media as developed in [43] (i.e., the initial gas pressure gradient cannot be sustained due to the rapid rate of advective transport through the material as compared to the slow transport of gas due to diffusion). Figure 12 displays the influence of the order of magnitude of the diffusivity of dissolved air in liquid-saturated cement paste on the dissolution kinetics when advection is considered.

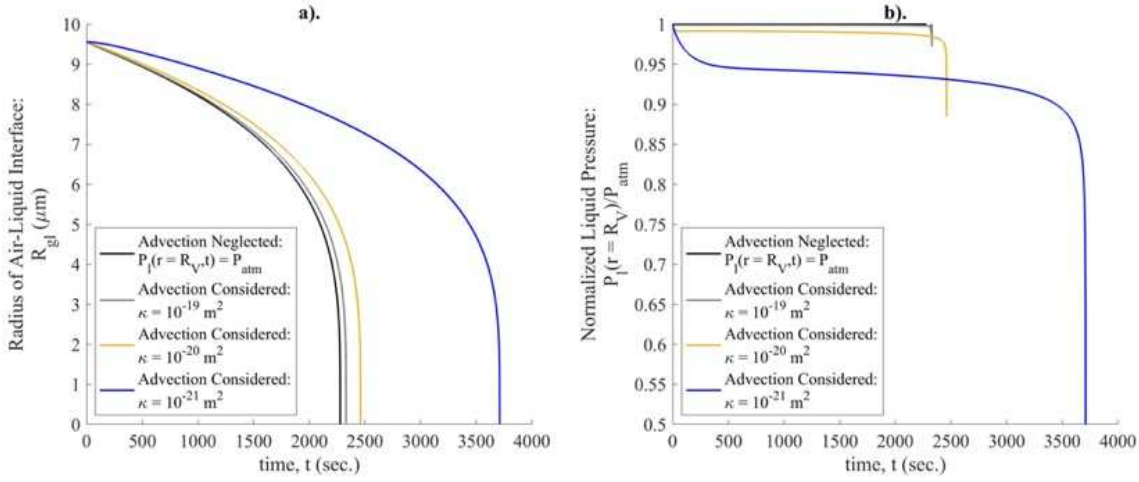

Figure 11: Influence of intrinsic permeability on time to complete dissolution of the trapped air. Model inputs: $m_t = 1$, $\theta = 0°$, $D_g^s = 5x10^{-12}$ m^2.s^{-1}, L = 1mm.

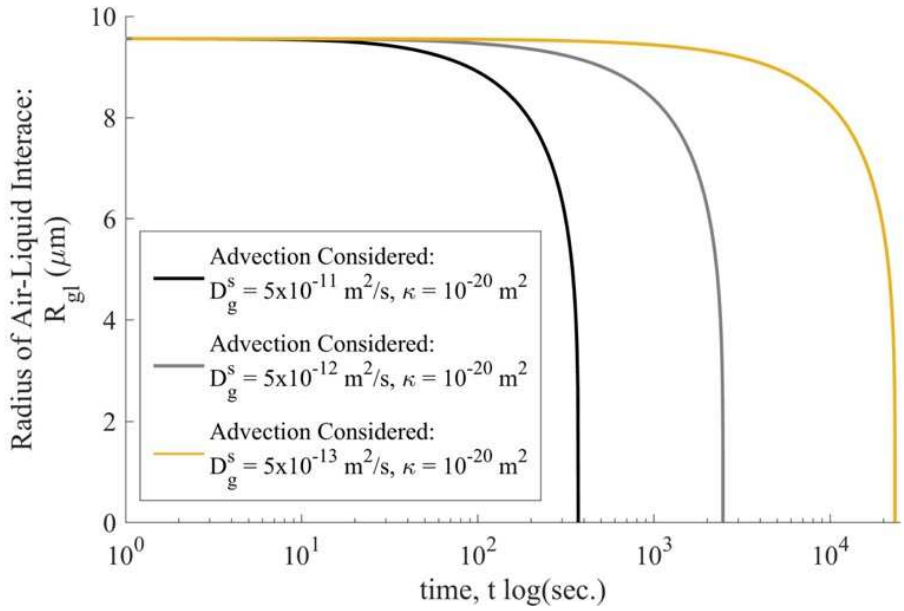

Figure 12: Influence of diffusivity of dissolved air in saturated hydrated cement paste on trapped air dissolution kinetics. Model inputs: $m_t = 1$, $\theta = 0°$.

3.3.3 Results on Time to Full Dissolution and Dissolution Kinetics

From the previously displayed outcomes and results, the influence in initially trapped mass of air, m_t, and the contact angle, θ, can be evaluated. Figure 13a displays a contour plot for time to full dissolution, when advection is considered, as a function of m_t and θ for a spherical void of radius 10μm and where the diffusivity D_g^s of dissolved air in the shell is equal to $5x10^{-12}$ m^2/s and the permeability κ is equal to 10^{-20} m^2. It can be clearly seen that the amount of trapped air significantly influences the total time to full dissolution whereas the effect of the contact angle to the time to full dissolution becomes notably pronounced when above a value of 20 degrees. Corresponding with Section 3.1, on Figure 13a we delimitate regions that are not physically possible under the assumption of a liquid pressure equal to the atmospheric pressure in the initial

state (in blue) and regions for which multiple initial geometries are possible (in pink). In this latter case, we chose the initial geometry with the lowest free energy (see Eq. 7) to calculate the time to full dissolution. Figures 13b to 13d evaluate other material and system inputs: values of intrinsic permeability, the diffusivity of dissolved air in saturated cement paste, and the air void size. Figure 14 displays examples of evolutions for various contact angles and Figure 15 displays the influence of the thickness, L, of surrounding cement paste shell and the spherical air void radius, R_V, on time to full dissolution, t_f, of the trapped gaseous air.

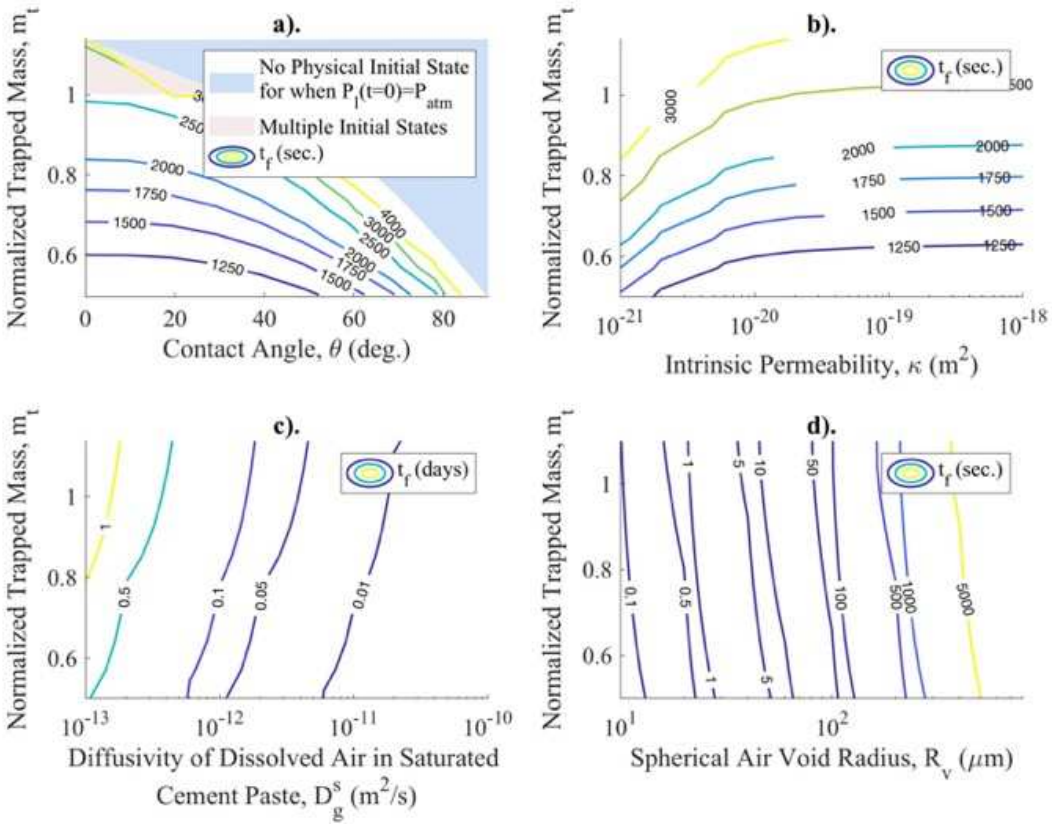

Figure 13: Time to full dissolution, t_f, contours of a large domain of normalized trapped mass, m_t, and a). contact angles, θ, where $R_V = 10\mu m$, $D_g^s = 5x10^{-12}$ m^2/s, $\kappa = 10^{-20}$ m^2, and L = 1mm, b). intrinsic permeability, κ, where $\theta = 0°$, $R_V = 10\mu m$, $D_g^s = 5x10^{-12}$ m^2/s, and L = 1mm, c).

671 diffusivity, D_g^s, where θ = 0°, R_V = 10μm, κ = 10^{-20} m^2, and L = 1mm, and d). air void radius,

672 R_V, where θ = 0°, D_g^s = 5x10^{-12} m^2/s, κ = 10^{-20} m^2, L = 1mm.

673

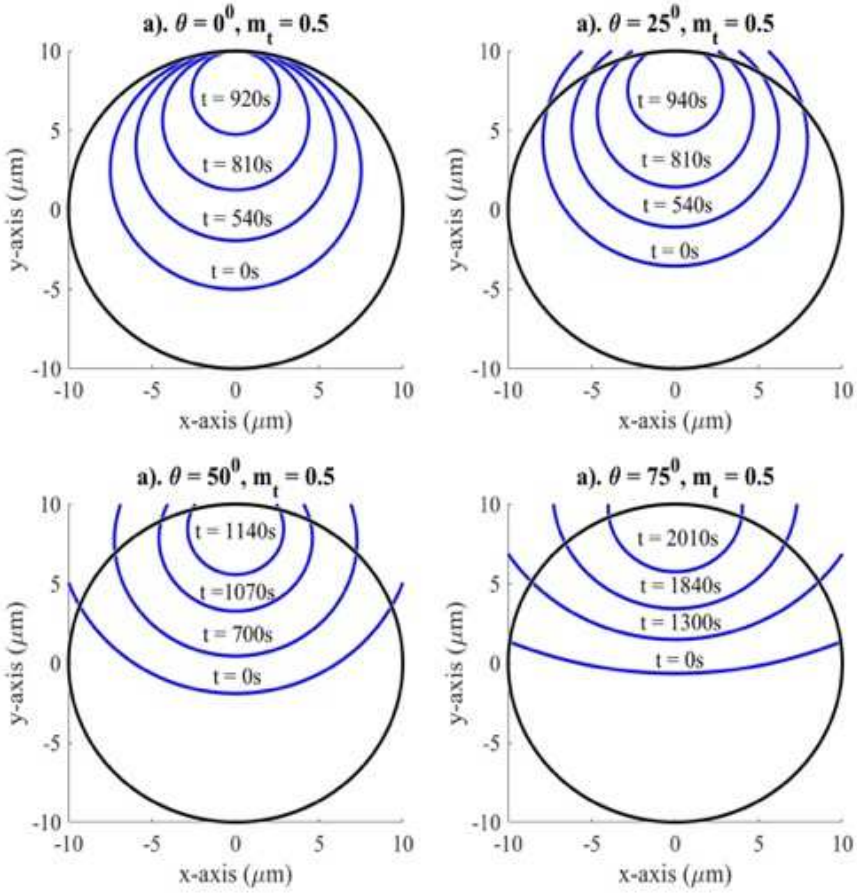

674

675 **Figure 14:** Examples of gas-liquid surface evolution for normalized trapped mass, m_t, of 0.5 and

676 various contact angles: a). 0°, b). 25°, c). 50°, d). 75°. Inputs: R_V = 10μm, D_g^s = 5x10^{-12} m^2/s,

677 and κ = 10^{-20} m^2.

678

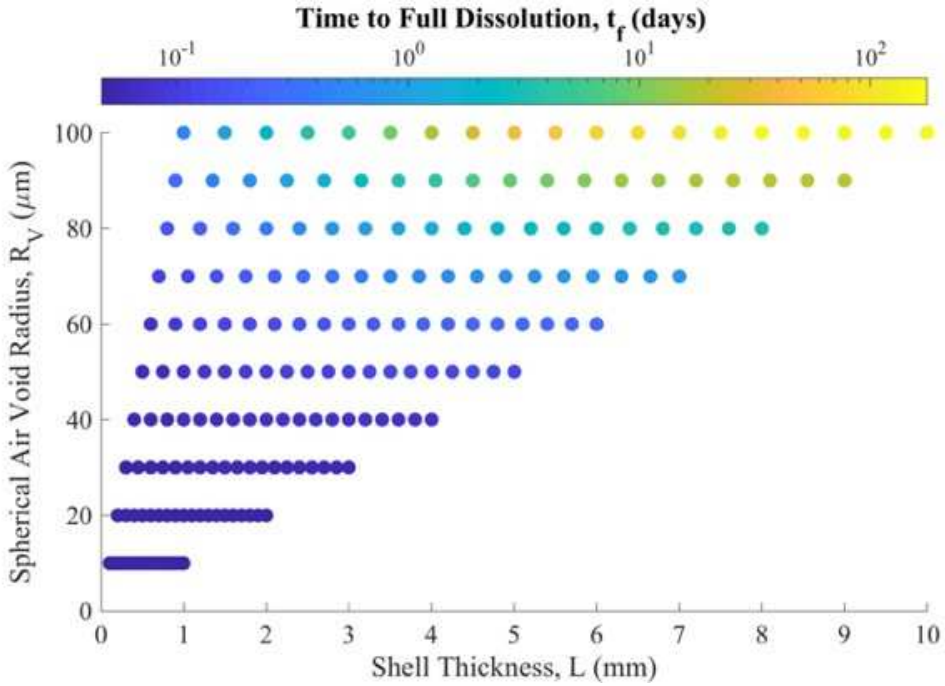

Figure 15: Influence of spherical air void radius, R_V, and porous solid shell thickness, L, on time to full dissolution for $m_t = 1$, $\theta = 0°$, $D_g^s = 5x10^{-12}$ m^2/s, and $\kappa = 10^{-20}$ m^2.

3.3.4 Comparison with Experimental Data

As discussed and displayed in Section 2.2.2 and Figure 5, fitting power law relationships to the temporal size reduction of the trapped air can provide significant insight into the governing physics of the model. For the following findings the fit relation is given by $R_{gl}(t) = A(B\text{-}t)^C$, where A is a constant, B represents the time to full dissolution, and C is the exponent of the power-law relation [33,34]. As displayed in Figure 16a, for systems with a zero contact angle (i.e. θ=0°), the determined power (i.e., value of C) is ~0.25, independent of whether advection is considered or neglected, and is found to be mostly independent of the initial trapped mass m_t. As a means of comparison, the Epstein-Plesset and experimental results for similar systems give a

693 power-law fit of ~0.33. The lower value found by the SVDK model is expected and its
694 explanation coincides with that given for the difference in solutions to the SVDK and Epstein-
695 Plesset model shown in Figure 9 (i.e., the concentration of dissolved gas in the liquid within the
696 air void is homogeneous and required to satisfy thermodynamic equilibrium of the air-liquid
697 interface which increases the rate of dissolution as compared to [17] leading to a lower value of
698 exponent in a power-law relation). Figure 16b displays a contour plot of fitted exponents of the
699 power-law relation for various values of m_t and θ. As expected, the power-law strongly depends
700 on the value of θ, which can be understood by the influence of Laplace pressure applied to the
701 system (i.e., for a larger value of θ larger values of R_{gl} are obtained, reducing the Laplace-driven
702 dissolution effects of the trapped air).
703

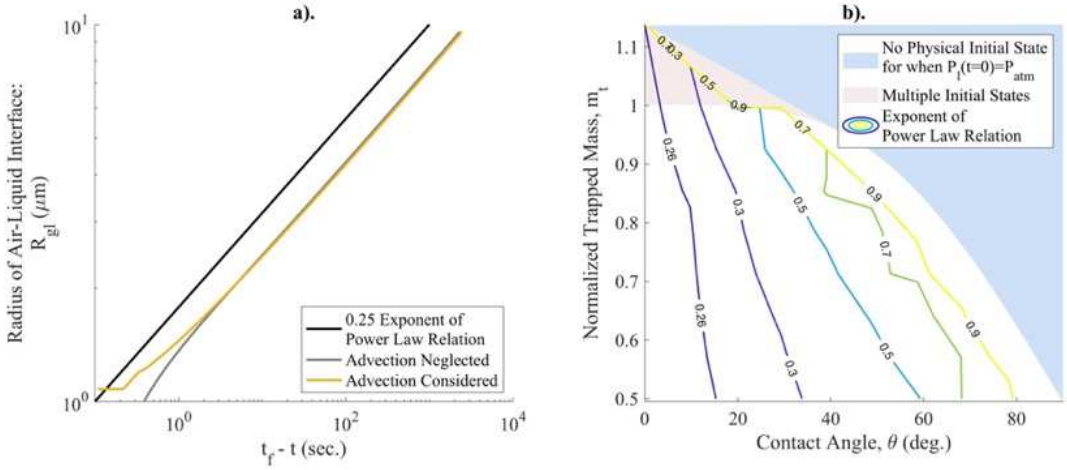

704

705 **Figure 16:** a). Power law evaluation for a system with θ = 0°, where R_V = 10μm and m_t = 1,for
706 when convection is neglected (i.e., not solved for) and considered, b). contour plot of power-law
707 exponents (i.e. values of C) as a function of contact angle for when advection is considered.
708

709 Having evaluated the general outcomes of the model and its comparison to proxy systems, it is
710 also of interest to understand how it relates to the experimental data that is available relating to
711 the long-term saturation of air void in cementitious materials. As initially presented in Section
712 2.2.1, Moradllo and Ley conducted a series of long-term ponding experiments [14] on cement
713 pastes with a similar pore structure used to formulate the model presented herein. A primary
714 conclusion was that after 60 days of ponding and within the first 6mm of the sample (i.e., depth
715 from the ponded surface) air voids with radii less than 100μm were found to be saturated
716 whereas larger air voids remained air-filled. Figure 17 displays that for acceptable values of D_g^s
717 and κ, it can be directly shown that air voids smaller than 100μm in radius will be completely
718 saturated, while voids larger than 100μm will remain partially air-filled. Similar to the
719 comparison made to the Epstein-Plesset model presented in Figure 9, this finding does not
720 directly validate the model but improves the likelihood that it is capturing the governing physics
721 of the phenomena, seeing as how it agrees very well within that same order-of-magnitude of each
722 comparison.
723
724 Also, it is important to note that if air-voids are well-spaced and do not influence the dissolution
725 kinetics of one-another, Figure 17 suggests that the air voids roughly fill in order of increasing
726 size, as postulated in [10]. This calculation neglected interactions between air voids. In real
727 systems, interactions may happen: small air voids, subjected to larger Laplace pressures, should
728 empty into larger air voids, akin to Oswald ripening. Therefore, in real materials, interactions
729 may make the air voids fill in order of increasing size in a still more pronounced manner.
730

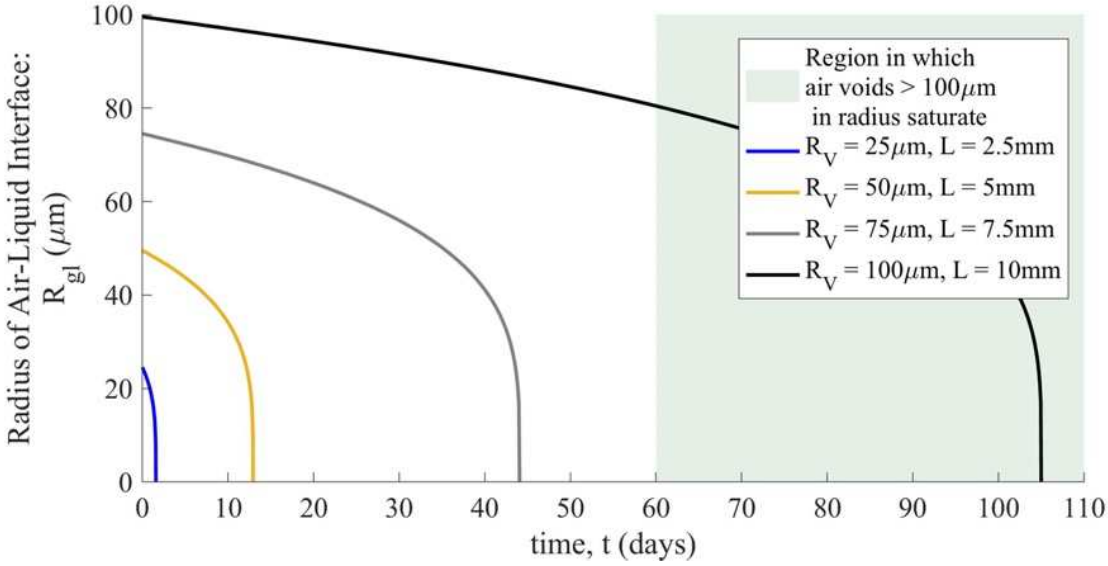

731

732 **Figure 17:** Comparison plot of SVDK model results with experimental conclusion from [14].

733 Model Inputs: m_t =1, $\theta = 0°$, $D_g^s = 1.5x10^{-12}$ m^2/s, and $\kappa = 10^{-20}$ m^2.

734

735 **3.3.5 Discussion on Impact of Initial Pressure Assumptions**

736

737 As mentioned in the formulation section, the previously presented results have assumed that at
738 time t = 0 the liquid pressure P_l at r = R_V, and within the spherical void, is equal to P_{atm} and the
739 gas pressure is then given by the Laplace Equation. It could also be reasonably assumed that the
740 gas pressure is equal to the atmospheric pressure P_{atm}. Figure 18a displays the outcomes of
741 setting the gas pressure initially equal to P_{atm} on the evolution of the radius of the air-liquid
742 interface and Figure 18b displays the evolution in liquid pressure at r = R_V. It is clear that the
743 assumption does not significantly influence the outcome due to the fact that the liquid pressure
744 gradient in the system quickly equilibrates, resulting in very similar dissolution kinetics of the
745 trapped gaseous air.

746

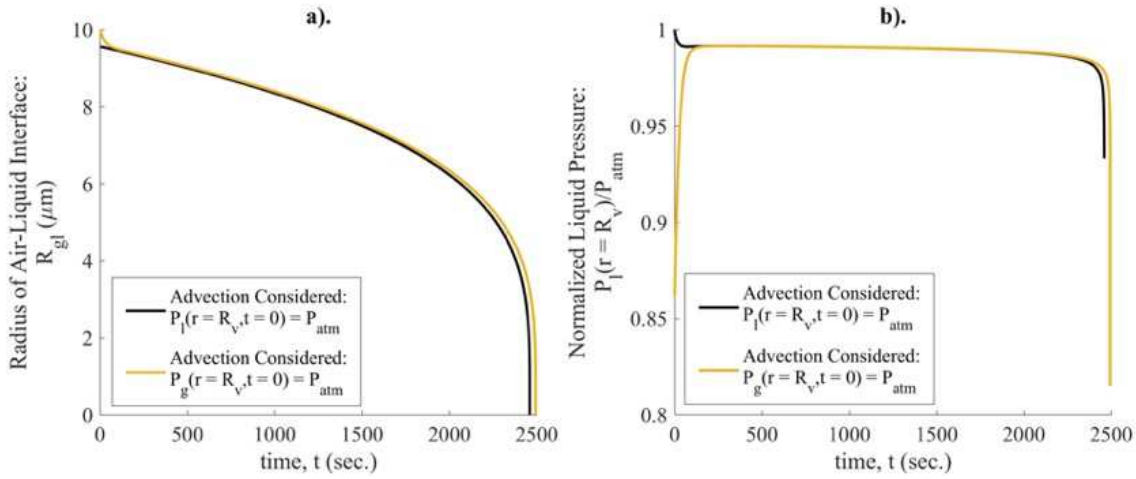

747

748 **Figure 18:** Assessment of initial liquid and gas pressures at r = R_V on dissolution kinetics of

749 trapped air. Model inputs: m_t =1, θ = 0°, $D_g^l = 5x10^{-12}$ m^2/s, and κ = 10^{-20} m^2, L = 1mm.

750

751 With the SVDK model, we looked at the time to full dissolution of pores that end up being fully

752 saturated with liquid. However, based on our theoretical considerations, it is possible that,

753 depending on the configuration of the gas-liquid interfaces right after capillary imbibition, some

754 air voids never fill fully with liquid, even if left indefinitely under water.

755

756 **4.0 SVDK Model Conclusions**

757

758 As displayed in the previous section, the formulated SVDK model advances the current state-of-

759 the-art in the field, reviewed in Section 2, by clearly detailing how single air voids become

760 liquid-saturated due to dissolution, diffusion, and advection of the trapped gaseous air. The

761 SVDK model results were compared to previous efforts [16,17,35] for simple systems (i.e. as

762 spherical gas bubble surrounded by an infinite amount of liquid) as shown in Figure 9 and found

763 to agree well in terms of solution form and the order of magnitude of time to full dissolution. As

noted, the departures in the results can be readily explained due to assumptions present in the model that are applicable to porous media with highly tortuous capillary porosity. Additionally, the SVDK model results were compared to experimental findings presented in [14] and found to agree very well. Outcomes of this comparison were also used to evaluate a postulation made by G. Fagerlund in [10] that the voids in cementitious material fill in order of increasing size – likely this is the case when considering a polydisperse air void system (i.e., small air voids preferentially diffuse into larger voids).

Along with the comparisons made to previous efforts, it was displayed how the SVDK model can evaluate the dissolution kinetics of trapped gases over a very large domain of trapped masses of air and contact angle in addition to the influence of when advection is considered and neglected. Notably, it was found that as the intrinsic permeability of the porous paste shell increased the SVDK model begins to approximate the solution when advection is not solved for (i.e., when the dissolution of the dissolved air in the porous shell is exclusively limited by diffusion). This finding, alongside the influence of the contact angle and value of the diffusivity on time to full dissolution, is significant as it provides novel insight into how such a system might behave and could be manipulated for design purposes. For example, using the outcomes of this model, the diffusivity and intrinsic permeability can be designed into the material through selection of appropriate values of water/cement (w/c) ratio and a minimal curing time, in the case of cementitious materials, and reliably provide a desired time to critical saturation. Also, by impacting the time to full dissolution, the contact angle between the pore solution and the solid surfaces could influence the freeze-thaw resistance, which might explain why hydrophobic agents can impact freeze-thaw durability of concrete [44].

Although the SVDK model has resulted in numerous insights into the slow saturation of air void in cementitious materials, its direct validation is still necessary. To do so, small specimens of air-entrained cement pastes could be prepared and evaluated using high resolution nanoCT as it saturates over time. The efforts and results found in a similar experiment [14] have provided insight into the global saturation of a sample, but it is necessary to study only a selection of air voids at finer time steps and resolution below 8.8μm/voxel in effort to see the evolution of the air-liquid interface. Additionally, it could be envisioned that a microfluidic device could be constructed as in [13] to provide similar insight and is left as future work.

The SVDK model answers how air voids saturate over time by the dissolution- and transport-driven collapse of trapped gaseous air. An extension could make it possible to understand and model 3D systems in which the air void system is polydisperse – allowing for the prediction of the long-term saturation rate, S_2, given a known air void size distribution and various material properties without assumptions on how air voids fill in relation to one another [10,24,25]. Additionally, it is important to note that the following work has been found to have a broad range of application and contribution. The dissolution of trapped gases has major relevance and significance in fields ranging from carbon capture [45] to drug delivery [46] and bioremediation [47], but is directed here to progress the field's understanding of how the long-term saturation rate of cementitious materials is linked to air void-scale phenomena.

5.0 Acknowledgments and Funding Sources

This material is based upon research supported by the Chateaubriand Fellowship of the Office for Science & Technology of the Embassy of France in the United States. Additionally, this work is based upon work supported under a Department of Energy, Office of Nuclear Energy, Integrated University Program Graduate Fellowship. The first author would like to thank his friends and colleagues at Ecole des Ponts ParisTech for their kind invitation, unwavering support, and continued collaboration. We also thank Prof. Daniel Bonn for pointing out the interest in looking at power-law evolutions of the dissolution dynamics.

6.0 References

[1] D.P. Bentz, M. a Ehlen, C.F. Ferraris, E.J. Garboczi, Sorptivity-based service life predictions for concrete pavements, 7th Int. Conf. Concr. Pavements–Orlando, Florida, USA, Sept. (2001).

[2] W. Li, M. Pour-Ghaz, J. Castro, J. Weiss, Water Absorption and Critical Degree of Saturation Relating to Freeze-Thaw Damage in Concrete Pavement Joints, J. Mater. Civ. Eng. (2012). doi:10.1061/(ASCE)MT.1943-5533.0000383.

[3] S.H. Smith, P. Suraneni, C. Qiao, K.E. Kurtis, W.J. Weiss, Service-life of Concrete in Freeze-Thaw Environments: Critical Degree of Saturation and Calcium Oxychloride Formation, Cem. Concr. Res. 122 (2019) 93–106.

[4] W.J. Weiss, Concrete Pavement Joint Durability: A Sorption-Based Model for Saturation, the Role of Distributed Cracking, and Calcium Oxychloride Formation, CONCREEP-10. (2015). doi:10.1061/9780784479346.025.

[5] R.M. Ghantous, H. Madland, J. Kwong, W.J. Weiss, Examining the Influence of the Degree of Saturation on Length Change and Freeze-Thaw Damage, Adv. Civ. Eng. Mater. 8 (2019) 20190001. doi:10.1520/acem20190001.

[6] C. MacInnis, J. Beaudoin, Effect of Degree of Saturation on the Frost Resistance of Mortar Mixes, ACI J. Proc. (1968) 203–208.

[7] G. Fagerlund, Critical degrees of saturation at freezing of porous and brittle materials, 1973. doi:10.14359/17604.

[8] G. Fagerlund, Significance of critical degrees of saturation at freezing of porous and brittle materials, Div. Build. Mater. Lund Univ. (1973).

[9] AASHTO PP 84-18: Standard Practice for Developing Performance Engineered Concrete Pavement Mixtures, Am. Assoc. State Highw. Transp. Off. (2018).

[10] G. Fagerlund, The long time water absorption in the air-pore structure of concrete, Div. Build. Mater. Lund Univ. (1993).

[11] C. Hall, W.D. Hoff, Topics in Water Transport, in: Water Transp. Brick, Stone Concr., 2009.

[12] Z. Liu, W. Hansen, Moisture uptake in concrete under freezing-thawing exposure, Mag. Concr. Res. (2016). doi:10.1680/jmacr.15.00193.

[13] N.A. Sahloul, M.A. Ioannidis, I. Chatzis, Dissolution of residual non-aqueous phase liquids in porous media: Pore-scale mechanisms and mass transfer rates, Adv. Water Resour. 25 (2002) 33–49. doi:10.1016/S0309-1708(01)00025-2.
[14] M. Khanzadeh Moradllo, Q. Hu, M.T. Ley, Using X-ray imaging to investigate in-situ ion diffusion in cementitious materials, Constr. Build. Mater. (2017). doi:10.1016/j.conbuildmat.2017.01.038.
[15] P.K. Mehta, P.J.M. Monteiro, Concrete: microstructure, properties, and materials, 2006. doi:10.1036/0071462899.
[16] P.B. Duncan, D. Needham, Test of the Epstein-Plesset Model for Gas Microparticle Dissolution in Aqueous Media: Effect of Surface Tension and Gas Undersaturation in Solution, Langmuir. 20 (2004) 2567–2578.
[17] P.S. Epstein, M.S. Plesset, On the Stability of Gas Bubbles in Liquid-Gas Solutions, Chem. Phys. 18 (1950) 1505–1509.
[18] S. Sirivithayapakorn, A. Keller, Transport of colloids in unsaturated porous media: A pore-scale observation of processes during the dissolution of air-water interface, Water Resour. Res. 39 (2003). doi:10.1029/2003WR002487.
[19] S. Kentish, J. Lee, M. Davidson, M. Ashokkumar, The dissolution of a stationary spherical bubble beneath a flat plate, Chem. Eng. Sci. 61 (2006) 7697–7705. doi:10.1016/j.ces.2006.08.071.
[20] G. Kapodistrias, P.H. Dahl, Scattering measurements from a dissolving bubble, Acoust. Soc. Am. 131 (2018) 4243–4251. doi:10.1121/1.3703060.
[21] J.I. Siddique, D.M. Anderson, A. Bondarev, Capillary rise of a liquid into a deformable porous material, Phys. Fluids. (2009). doi:10.1063/1.3068194.
[22] K.M. Masoodi, R., Pillai, Wicking in porous materials: traditional and modern modeling approaches, Taylor and Francis Group, 2012.
[23] X. Li, S. Chen, Q. Xu, Y. Xu, Modeling capillary water absorption in concrete with discrete crack network, J. Mater. Civ. Eng. 30 (2018) 04017263. doi:10.1061/(ASCE)MT.1943-5533.0002122.
[24] D. Eriksson, T. Gasch, A. Ansell, A Hygro-Thermo-Mechanical Multiphase Model for Long-Term Water Absorption into Air-Entrained Concrete, Transp. Porous Media. (2018). doi:https://doi.org/10.1007/s11242-018-1182-3.
[25] Z. Liu, W. Hansen, A geometrical model for void saturation in air-entrained concrete under continuous water exposure, Constr. Build. Mater. (2016). doi:10.1016/j.conbuildmat.2016.07.113.
[26] W. Jason Weiss, R.P. Spragg, O. Burkan Isgor, M. Tyler Ley, T. Van Dam, Toward performance specifications for concrete: Linking resistivity, RCPT and diffusion predictions using the formation factor for use in specifications, in: High Tech Concr. Where Technol. Eng. Meet - Proc. 2017 Fib Symp., 2017. doi:10.1007/978-3-319-59471-2_235.
[27] T.C. Powers, T.F. Willis, The Air Requirement of Frost-Resistant Concrete, Proc. Twenty-Ninth Annu. Meet. Highw. Res. Board. (1949).
[28] ASTM C666/C666M - 15: Standard Test Method for Resistance of Concrete to Rapid Freezing and Thawing, 2015.
[29] J. Bentz, D P, Ferraris, C.F., Wingpigler, Service Life Prediction for Concrete Pavements and Bridge Decks Exposed to Sulfate Attack and Freeze-Thaw Deterioration, Volume II-Technical Basis for CONCLIFE- Sorptivity Testing and Computer Models, Building and

Fire Research Laboratory, National Institute of Standards and Technology, 2001.
[30] C.L. Lucero, D.P. Bentz, D.S. Hussey, D.L. Jacobson, W.J. Weiss, Using Neutron Radiography to Quantify Water Transport and the Degree of Saturation in Entrained Air Cement Based Mortar, in: Phys. Procedia, 2015. doi:10.1016/j.phpro.2015.07.077.
[31] X. Li, Y. Wang, B. Zeng, Y. Li, H. Tan, H.J.W. Zandvliet, X. Zhang, D. Lohse, Entrapment and Dissolution of Microbubbles Inside Microwells, Langmuir. 34 (2018) 10659–10667. doi:10.1021/acs.langmuir.8b02173.
[32] M. Buchgraber, A.R. Kovscek, L.M. Castanier, A Study of Microscale Gas Trapping Using Etched Silicon Micromodels, Transp. Porous Media. 95 (2012) 647–668. doi:10.1007/s11242-012-0067-0.
[33] O. Carrier, N. Shahidzadeh-Bonn, R. Zargar, M. Aytouna, M. Habibi, J. Eggers, D. Bonn, Evaporation of water: evaporation rate and collective effects, J. Fluid Mech. 798 (2016) 774–786. doi:10.1017/jfm.2016.356.
[34] E. Jambon-Puillet, N. Shahidzadeh, D. Bonn, Singular sublimation of ice and snow crystals, Nat. Commun. 9 (2018) 1–6. doi:10.1038/s41467-018-06689-x.
[35] P.B. Duncan, D. Needham, Microdroplet dissolution into a second-phase solvent using a micropipet technique: Test of the epstein-plesset model for an aniline-water system, Langmuir. 22 (2006) 4190–4197. doi:10.1021/la053314e.
[36] E.W. Weisstein, Sphere-Sphere Intersection, MathWorld - A Wolfram Web Resour. (n.d.). http://mathworld.wolfram.com/Sphere-SphereIntersection.html.
[37] D.N. Espinoza, J.C. Santamarina, CO2 Breakthrough - Caprock Sealing Efficiency and Integirty for Carbon Geological Storage, Greenh. Gas Control. 66 (2017) 218–229.
[38] M. Zhang, Y. He, G. Ye, D.A. Lange, K. Van Breugel, Computational Investigation on Mass Diffusivity in Portland Cement Paste Based on X-ray Computed Tomography, Constr. Build. Mater. 10 (2012) 472–481.
[39] H. Derluyn, P. Moonen, J. Carmeliet, Modelling of Moisture and Salt Transport Incorporating Salt Crystallizattion in Porous Media, Proc. CONMOD'08. (2008).
[40] N. Bignell, The Effect of Dissolved Air on the Density of Water, Metrologia. 19 (1983) 57–59.
[41] J. Sercombe, R. Vidal, C. Gallé, F. Adenot, Experimental study of gas diffusion in cement paste, Cem. Concr. Res. 37 (2007) 579–588. doi:10.1016/j.cemconres.2006.12.003.
[42] G. Ye, Percolation of capillary pores in hardening cement pastes, Cem. Concr. Res. 35 (2005) 167–176. doi:10.1016/j.cemconres.2004.07.033.
[43] O. Coussy, Mechanics and Physics of Porous Solid, 1st ed., Wiley, 2010.
[44] Z. Liu, W. Hansen, Effect of hydrophobic surface treatment on freeze-thaw durability of concrete, Cem. Concr. Compos. 69 (2016) 49–60.
[45] T. Cubaud, M. Sauzade, R. Sun, CO2 Dissolution in Water Using Long Serpentine Microchannels, Biomicrofluidics. 6 (2012).
[46] M. Azmin, G. Mohamedi, M. Edirisinghe, E.P. Stride, Dissolution of coated microbubbles: The effect of nanoparticles and surfactant concentration, Mater. Sci. Eng. C. 32 (2012) 2654–2658.
[47] V.A. Fry, J.S. Selker, S.M. Gorelick, Experimental investigations for trapping oxygen gas in saturated porous media for in situ bioremediation, Water Resour. Res. 33 (1997) 2687–2696. doi:10.1029/97WR02428.